A BIO-INSPIRED FINGERTIP

3D Printed Surface Patterns and Their Role in Surface Friction: An Experimental Study

R.R. Martoredjo

Delft University of Technology

A BIO-INSPIRED FINGERTIP

3D Printed Surface Patterns and Their Role in Surface Friction: An Experimental Study

by

R.R. Martoredjo

in partial fulfilment of the requirements for the degree of

Master of Science
in Mechanical Engineering

at the Delft University of Technology,
to be defended publicly on Monday November 11, 2019 at 10:00 AM.

Thesis committee:	Prof. dr. ir. P. Breedveld,	TU Delft, Chairman
	Dr. ir. D. H. Plettenburg,	TU Delft, External Committee Member
	Ir. J. S. Cuellar Lopez,	TU Delft, Daily Supervisor
	MSc. C. Culmone,	TU Delft, Daily Supervisor

THE ROAD NOT TAKEN

Two roads diverged in a yellow wood,
And sorry I could not travel both
And be one traveler, long I stood
And looked down one as far as I could
To where it bent in the undergrowth;

Then took the other, as just as fair,
And having perhaps the better claim,
Because it was grassy and wanted wear;
Though as for that the passing there
Had worn them really about the same,

And both that morning equally lay
In leaves no step had trodden black.
Oh, I kept the first for another day!
Yet knowing how way leads on to way,
I doubted if I should ever come back.

I shall be telling this with a sigh
Somewhere ages and ages hence:
Two roads diverged in a wood, and I-
I took the one less traveled by,
And that has made all the difference.

— Robert Frost, 1916

ABSTRACT

In the field of prostheses, significant developments have been accomplished so far in low-cost prosthetic limbs using 3D printing technology. However, when it comes to prosthetic hands, 3D printed prosthetic hands are still limited in their grasping ability, such as the adaptability to the shape of an object and a sufficient pinch force level for practical use. The goal of this experimental study is to engineer a bio-inspired surface structure to improve the grip action of prosthetic hands. The low-cost FDM 3D printing technology in combination with the flexible material, Thermoplastic Polyurethane (TPU) 95A, was evaluated for this purpose. 3D printed surface (deformable) patterns were printed on top of a flat, rigid surface. The 3D printed patterns consisted of pillars or lines with varying thickness *d*, tip thickness *D*, wavelength λ, and curvatures α that were combined into different patterns. The frictional characteristics of the 3D printed patterns were assessed for nine different test scenarios, i.e. three different loads F_N against three different countersurfaces. Despite the small differences in the static coefficient of friction μ_s of the 3D printed patterns, some consistent trends were found. First, μ_s increases with increasing thickness *d*. Second, μ_s increases with increasing wavelength λ up to a point in which the decrease of number density of the 3D printed features decreases the overall friction. Third, μ_s increases for pattern curvatures with peaks in the opposite direction, such as wave or circular patterns. Lastly, μ_s decreases under increasing normal load F_n. The surface patterns were tested on the fingertips of a 3D printed prosthetic hand. The fingertips were assessed using the Box and Blocks Test (BBT), in which the pattern with the highest score displayed an ~70% increase in the number of blocks moved, compared to the original rigid fingertip of the 3D printed prosthetic hand in question. Further research and development are essential, especially for the FMD 3D print process of small dimensional printing in combination with flexible materials. Nevertheless, the proposed fingertip pattern demonstrated a first step towards future improvements of the grip action of low-budget 3D printed prosthetic hands using soft fingertip patterns.

CONTENTS

1. INTRODUCTION

1.1. Prosthetic Hands

The lack of medical supplies, laboratory equipment, and prostheses in developing countries renders the need for challenging these healthcare issues. Three-dimensional (3D) printing may provide accessible and functional parts, improving health care across developing countries. The key principle of Additive Manufacture (AM), generally referred to as 3D printing, is the use of a digital model to build 3D parts in a layer-by-layer fashion. 3D printing technology were only suitable for prototyping, in the early stage. However, 3D printing is rapidly transforming into a production technology used in variety of major industries, such as aviation, automotive, construction, healthcare and fashion [1]. 3D printing offers many advantages, such as the possibility to fabricate complex geometries and to reduce material costs, process steps, production time and labour cost. Compared to traditional manufacturing techniques, where highly skilled people are typically required, 3D printing generally does not need any particular manual skills. With the rapid improvement of 3D printing technology, many 3D printers entered a wider range of industries, making this low-cost method of part production significant easier to access [1, 2].

In the field of prostheses, many devices are usually developed using expensive high-tech features. However, most people, especially in developing countries, are in need of low-cost easily manufactured prostheses. Several organisations have already shown the possibility to manufacture low-cost high-tech prosthetic limbs using 3D printing. A successful example is the prosthetic arm produced by the company called “Not Impossible”, which specializes in tackling healthcare issues using low-cost, open-sources methods. However, post-assembly steps and thus trained people are still required to make these prosthetic devices [3]. Recently, the first fully non-assembly prosthetic hand has been successfully developed, using 3D printing [4]. This non-assembly approach strives towards increasing the accessibility of prostheses in developing countries by reducing the current post-processing steps. However, conventional prosthetic hands are still limited in their grasping ability, such as the adaptability to the shape of an object and a sufficient pinch force level for practical use [5]. In addition, the pinch force generated by the non-assembly 3D printed prosthetic hand is significantly lower (<15N) compared to commercial prosthetic hands [4]. The finger configuration in conventional prosthetic hands is primarily related to the geometric shape of the grasped object. The automatic folding of the fingers around a shape demand accurate grasping and a high pinch force to secure an object [5]. Moreover, these finger(tip)s generally consist of rigid materials. On the contrary, the human hand consists of an active fingertip-based configuration due to the soft skin, which behaves more like rubber than rigid material. This behaviour results in the effective distribution of the pinch force at the fingertip [6]. The most common grip for object precision-manipulation research is the act of grasping an object between the index finger and the thumb, known as the (precision) pinch grip. To prevent slipping of an object, precise control of the fingertips is necessary.

In the past decade, considerable effort has been devoted by researchers to study human skin. With the development of bio-inspired materials, the behaviour of skin friction has gained increasing interest in the field of engineering tribology. Tribology, which comes from the Greek word Tribos meaning ‘science of friction’, is the science and the engineering of interacting surfaces in relative motion. Recent tribological studies have investigated the role of fingertip skin friction in human prehension (action of grasping). It is well established that the effective friction solutions regarding the human skin-surface tribology make for an interesting approach to improve prosthetic prehension [7, 8, 9]. However, the exact contribution of skin friction at the fingertip is still elusive. Understanding the role of (skin) friction during object manipulation can be the next step in improving the grip action of prosthetic hands.

1.2. Human Finger Anatomy

The complex anatomy of the human hand is evident to carry out various complex tasks efficiently. These tasks require complicated movements with fine controlled forces. The relationship between different soft tissue structures contributes to the hand's ability to grasp a variety of objects accurately [10]. The human finger consists of bones, tendons, and ligaments. The tendon is a fibrous connective tissue that connects the muscle to the bone. The ligament is a supportive tissue that connects bone to bone. The skeleton of the hand can be divided into three sections: the wrist, the palm, and the phalanges. The phalanges are the bones within the fingers. Except for the thumb, each finger comprises of three bones. Starting from the proximal (closest to the palm) to distal (the tip of the finger), the bones of each finger are known as; the proximal phalange (PP), the middle – or intermediate – phalange (MP) and the distal phalange (DP). The thumb has no middle phalange, giving a total of 14 phalanges in the human hand. The joints between the phalanges, referred to as the knuckles, allow for the rigid bodies to move relative to each other. The first and largest knuckle is the joint between the hand and the finger, referred to as the metacarpophalangeal joint (MCP); the second knuckle is the proximal inter-phalangeal joint (PIP); and the farthest knuckles is the distal inter-phalangeal joint (DIP), Figure 1.1 [10].

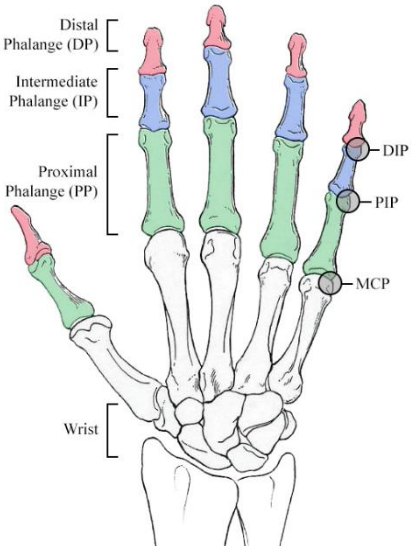

Figure 1.1. Bones and joints of the human hand with the indicated knuckles: metacarpophalangeal (MCP), interphalangeal (PIP), and inter-phalangeal (DIP), adapted from [11].

The contraction of the hand muscles plays a role in the modulation of the shape of the hand. However, there are no muscles located in the finger. The movement of the finger takes place when the muscles (i.e., in the hand and forearm) pull on the tendons in the finger. Detailed information about the joints, muscles, and tendons in the hand, are addressed by Schreuders et al. [10].

The human fingertip consists of various components, such as the bone, pulp, fingernail, and skin, Figure 1.2. The variation in softness can classify these components. The bone and nail are rigid compared to the soft deformable tissue of the pulp and skin. Therefore, the fingertip can be defined as a hybrid structure which consists of soft and hard components. The soft components of the fingertip allow safe interaction with surrounding objects by adapting to the shape. In addition, softness alone limits the weight that can be grasped by the hand, thus concluding the function of the rigid finger bones [12]. The fingernail is located at the tip of the finger. The nail protects the distal phalange and the surrounding soft tissue at the fingertip. Moreover, the nail enhances precise, delicate movements of the finger through counterpressure exerted on the pulp. Finally, the nail also functions as a so-called "extended precision grip", which makes it possible to e.g., pull out a splinter [13].

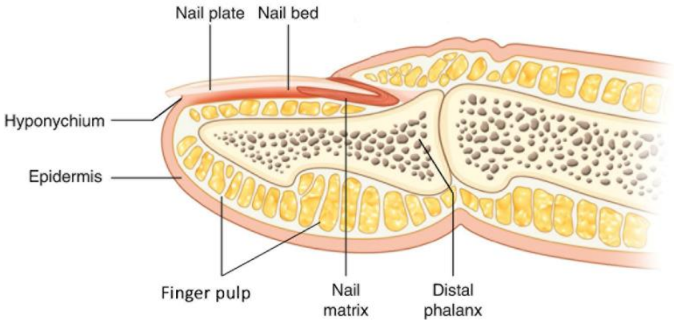

Figure 1.2. Fingertip anatomy, adapted from [14].

The mechanical behaviour of the finger pad plays an essential role in object manipulation. The finger pad is a specific region of complex, nonlinear soft tissue on the palmar side of the fingertip. The mechanical properties of the finger pad influence the stress/strain relation of the skin and underlaying tissues. The skin is a multi-layer structure in which each layer consists of different composition, thickness, and hydration. This results in layers with different tissues and mechanical properties. The human skin is comprised of two primary layers: the outer epidermal layer (epidermis) and the dermal layer (dermis). The epidermis is thin (close to 1 mm), flexible and hard, and offers resistance to stretch and wear. The epidermal is thicker at the palm (369 µm) and at the fingertip (429 µm), compared to the rest of the arm such as the back of the hand (84.5 µm) or the forearm (43.9 µm). The thicker epidermal layer leads to a tougher skin that is able to transfer the forces to the bones. The epidermis consists of various sub-layers of which the stratum corneum (SC) is the outermost sub-layer. The softer dermis, beneath the epidermis, consists of elastin component responsible for the elastic properties of the skin. Beneath the dermis lies the very soft vascular hypodermis (or pulp) tissue, which consist of connective tissue that attaches the skin to the underlying bone and muscles. The tissue is primarily composed of fat cells which contribute to the firm rounded shape of the finger and its adaptability to the shape of an object, Figure 1.3 [10, 15, 16]. The combined behaviour of the skin (and pulp) layers determines the behaviour of the skin under load. Therefore, no specific tribological mechanical value can be given for the skin [17].

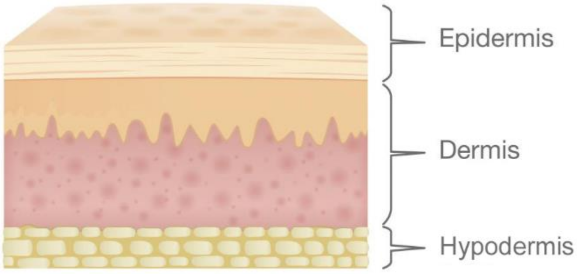

Figure 1.3. Skin layers (i.e., epidermis, dermis) and the hypodermis tissue beneath the skin, adapted from [18].

1.3. Fingerprint Pattern

The finger pad of a human fingertip is characterized by concentric friction ridges (raised), valley, and sweat pores. The ridges, separated by valleys, create a unique pattern better known as the fingerprint. At a global level, the frequency and orientation field of the ridges are the fundamental features of the fingerprint pattern. Ridges vary in width from 300 – 400 µm, with a ridge/valley periodical distribution of 500 – 680 µm [19, 20]. Fingerprint patterns are generally classified into three primary types. These primary patterns occur at different frequencies in the human population: arches (17.4%), loops (52.2%) and whorls (30.4%) [21], Figure 1.4. The arch pattern is characterized by ridges that enter one side and flow out the other side while rising in the middle, Figure 1.4a. The loop pattern is the most common pattern and contains a recurve, a delta – i.e., a point on or in front of a diverging ridge which can be a dot or a short ridge – and several ridges between the delta and core, Figure 1.4b. The whorl pattern is characterized by ridges resembling small whirlpools swirling around a point, Figure 1.4c. Detailed information on fingerprint patterns and their technical terms are addressed by Moayer et al. [22].

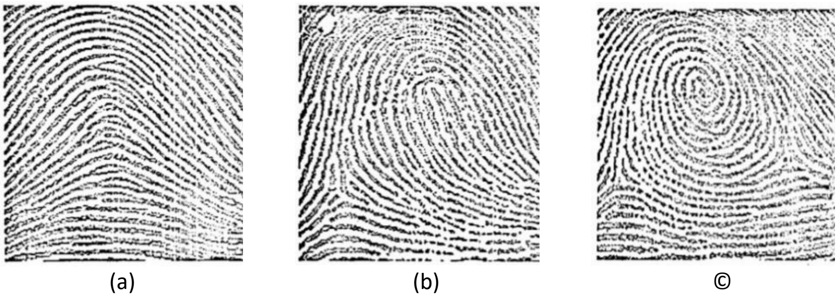
(a) (b) ©

Figure 1.4. Primary fingerprint patterns: (a) arch pattern, (b) loop pattern, (c) whorl pattern [22].

At a local level, other distinguishing features, the minutiae points, can be found in the fingerprint patterns. The minutiae points refer to different ways the ridges can be discontinuous. They include characteristics such as the end of a ridge (termination), or separation of a single ridge into two ridges (bifurcation) [23]. The width, height, and length of each ridge change when compressed, decompressed and/or stretched. When compressed, the flattened ridges create a uniform contact surface. This configuration limits the deformation of the ridges and increases the fingertip stiffness [24]. Limited studies have indicated that the skin along the friction ridges is locally stiffer than across the ridges, which results in a direction-dependent deformation of the fingertip [25, 26]. Besides, it is believed that the grip increases perpendicular to each ridge and leads to an increase in grip in all direction due to the concentric pattern of the ridges at the fingertip. However, the exact role of the fingertip patterns is not yet fully understood.

1.4. Examples of Biological Adhesive Surfaces

Optimization of (dry) adhesion in climbing animals is a result of combined strategies at different scale levels. The biological adhesive structures found in gecko toe pads, spiders, and insects consist of hairy structures (setae) whose hierarchical surface topology (texture) and material properties influence adhesion [27]. In this paragraph, we take a closer look at the optimization strategies of biological adhesive surfaces. The adhesive pads of insects allow them to attach to a variety of surfaces securely [28]. In many cases, hierarchical structures are observed to allow for ‘contact splitting’; large contacts are split into smaller ones, Figure 1.5. For example, the gecko toe pads have several structural levels. Thousands of setae (30-130 µm long, 50-10 µm thick), are branched into secondary seta (2-3 µm long, 0.2-0.3 µm thick). The secondary setae, in turn, consist of spatula structures (100-200 nm long, 5-20 nm thick) [29]. With the setae’s ability to deform, hierarchical structures allow adaptability to rough surfaces and uniform distribution of stress [27].

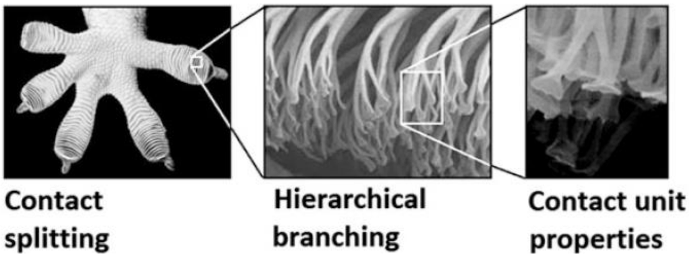

Figure 1.5. Multiscale mechanism of the biological adhesive structure of gecko pads: (a) contact splitting, (b) hierarchical branching, (c) contact unit properties (i.e. tapering or grading of mechanical properties) [27].

Setae display gradients of mechanical properties and a contact unit for optimized adhesion [27]. For example, the setae tips of the ladybird beetle contain high amounts of soft rubber-like protein. These proteins can bind with a high amount of water, thereby changing the mechanical properties of the setae; a 6000-fold increase in Young's modulus of the setae tips has been observed after drying [28]. In addition, the geometric shapes of setae influence the resulting mechanical properties. A narrowing diameter at the neck of setae reduces the local bending stiffness, allowing the tip to bend to achieve better attachment to an uneven surface [29], Figure 1.6.

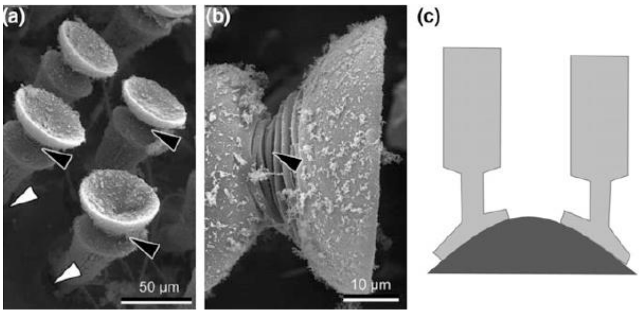

Figure 1.6. The adhesive microstructure in dytiscid beetle *Dytiscus Marginalis*: (a) the white arrowheads indicate the base of the stalk, (b) the black arrowheads indicated the narrowing neck structure, (c) diagram of the forming contact between micropillars (light grey) with narrowing neck and a rough surface (dark grey) [29].

The contact unit of the setae has been observed to determine its adhesion abilities. For example, the discoidal (or mushroom-like) geometry of setae tips of male beetles (Figure 1.7d) generates much higher adhesion on smooth surfaces compared to the females' ones (Figure 1.7a-c). This difference is because the discoidal geometry, found at the setae tips of male beetles, results in a geometry-induced homogenous stress distribution [28].

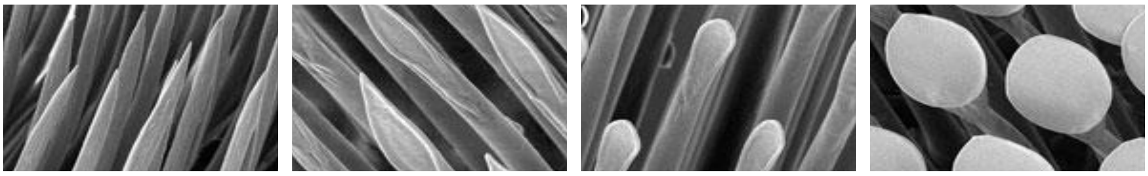

Setae with pointed tips

(a)

Setae with lanceolate tips

(b)

Setae with a flattened and rounded, spatula-shaped tips

(c)

Setae terminated with discoidal terminal elements

(d)

Figure 1.7. The hairy attachments of the ladybird beetle *Coccinella Septempuctata*. The legs of a female beetle are ventrally covered by different types of setae (a-c). The legs of a mal beetle are also ventrally covered by setae types shown in (a) and (b) but have an additional type (d) [28].

1.5. Goal of the Study

The goal of this experimental study is to engineer a bio-inspired surface structure to improve the grip action of prosthetic hands and to evaluate the low-cost 3D printing technology for this purpose. The 3D printed surface structures will be engineered with the idea of future integration with 3D printed prosthetic hands, such as presented by Cuellar et al. [4]. In this experimental study, the emphasis will be on analysing the frictional characteristics of soft, deformable surface patterns by systematically modifying topographical features at the surface. Biophysical principles, such as the contact properties and surface topography, have been optimized in nature. Therefore, the skin at human fingertips and superior (dry) adhesive surface structures of animals were studied.

1.6. Outline

The paper is organised as follows: Chapter 1 provides an introduction in 3D printed prosthetic hands, the anatomy of the human fingertip, and the adhesive surface structures of animals. In Chapter 2, the theoretical background on surface friction will be introduced. In Chapter 3, the design principles based on bio-grasping methods will be introduced. The design approach, conceptual design, and final friction test of the 3D printed surface patterns are described in Chapter 4 to Chapter 9. In Chapter 10, the functional testing of the 3D printed surface patterns on a prosthetic hand will be discussed. Finally, the discussion and the conclusion are given in Chapters 11 and 12, respectively.

2. FRICTION

2.1. Surface Terminology

Friction force provides resistance to the relative motion between two surfaces. Friction can either be static (starting) or dynamic (moving) [30]. Tribological studies have indicated the importance of skin friction behaviour in humans' ability to grasp and manipulate objects. However, research on skin friction is highly intricate due to the complex structure of human skin. Surface Engineering is a sub-category of Material Science which focuses on the surface of solid matter. A solid matter consists of a specific arrangement of atoms, which do not flow like a liquid or gas. In addition, a solid matter is able to withstand forces exerted perpendicular or parallel to the surface. The skin can be defined as a soft, solid matter. In order to get a better understanding of the skin-surface tribology, the following terminology needs to be clarified [31]:

- **Surface texture** (or surface topography) comprises the small, local deviations of a real surface from the perfectly flat, ideal surface. The sequence of peaks-and-valleys generally results in an increased surface area. The surface texture is defined by the direction of the *surface pattern* and the *surface roughness* [31, 32].

- **Surface pattern** comprises the direction of lines and/or shapes (e.g., vertical, horizontal, circular) and the periodic deviations of a surface, referred to as waviness, on a macroscopic scale, Figure 2.1 [31, 32].

- **Surface roughness** represents the surface irregulates, which is characterized by micro-geometric *asperities* of varying amplitudes and spacing, Figure 2.1. The larger these deviations, the rougher the surface. Surface roughness is an important parameter, for the tribological behaviour of surfaces, which can increase the friction through the interlocking or deformation of the asperities [32].

- **Asperities** are defined as the 'unevenness of a surface', on a microscopic scale. Smooth surfaces are generally not totally smooth on a microscopic scale but consist of asperities. Each asperity comprises of a local peak and adjoining valley, Figure 2.1. The surface asperities have been correlated with friction. However, their relationship is complex and still poorly understood [33].

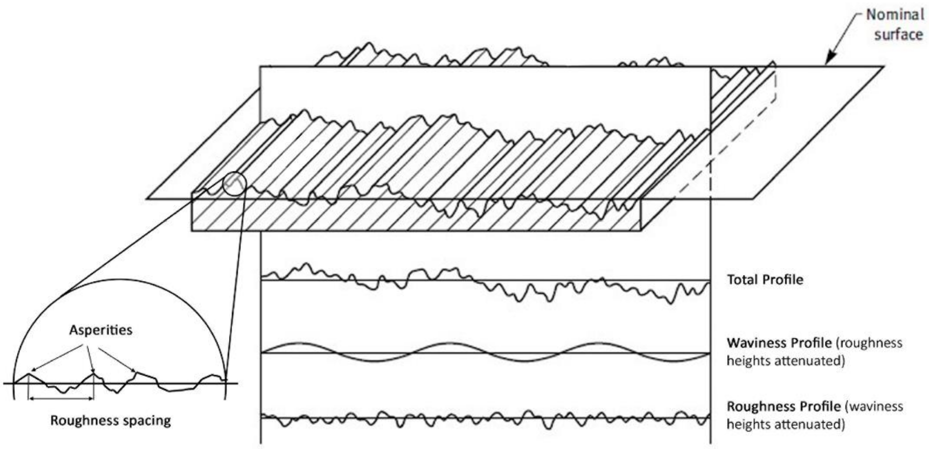

Figure 2.1. Surface texture (or surface topography) parameters of solid surface structures, adapted from [34].

- **Macroscopic scale** refers to a length scale over 1 mm; for example, such as the behaviour of the gross of the body, in which the behaviour of micro-asperities gets combined [35].

- **Microscopic scale** refers to a length scale (l) of 1 µm ≤ l ≤ 1 mm; for example, in which the phenomenon of the mechanical interlocking of asperities during friction can be observed [35].

2.2. Theoretical Background

Biological surfaces are relatively different compared to engineering surfaces. Nevertheless, some existing models of bio-inspired surfaces are described using terminology initial introduced for models of engineering surfaces [35]. This is also the case for skin friction. Skin is defined by nonlinear, viscoelastic material properties, similar to those of an elastomer. Therefore, skin friction is generally expressed as the two-term theoretical friction model of elastomers [31, 36]:

$$\mathrm{F_{f,tot}} = \mathrm{F_{f,adh}} + \mathrm{F_{f,def}} \qquad (1)$$

Which gives the friction force as the sum of an adhesion term $\mathrm{F_{f,adh}}$ (considered as the main contribution of skin friction) and a deformation term $\mathrm{F_{f,def}}$. The adhesion component of skin friction will be further referred to in this paper as the adhesion of skin. Generally, adhesion occurs when two surfaces are in contact. When two macroscopically smooth surfaces are in contact, they initially touch micro-geometric asperities. These surface asperities deform through elastic and plastic modes, thus increasing the contact area. The forming junctions between these asperities depend on the physical and chemical characteristics of both surfaces. The adhesion can be calculated from the shear strength τ and the real (or true) contact area $\mathrm{A_{real}}$ [36]:

$$\mathrm{F_{f,adh}} = \tau \cdot \mathrm{A_{real}} \qquad (2)$$

The real contact area, refers to the sum of all friction-generated contact points between two surfaces [37], is influenced by surface texture, mechanical properties, and loading conditions [17]. The $\mathrm{A_{real}}$ (on a microscopic scale) is generally far less compared to the commonly measured apparent contact area $\mathrm{A_{pp}}$ (on a macroscopic scale). Therefore, to determine the skin friction, the $\mathrm{A_{real}}$ is significantly more important than the $\mathrm{A_{pp}}$. However, the $\mathrm{A_{real}}$ of the human fingertip is rather difficult to measure, especially if it does not involve contact with a smooth surface [38]. The deformation term of skin friction $\mathrm{F_{f,def}}$ arises from mechanical hysteresis due to the viscoelasticity of the skin and an additional interlocking mechanism attributed by the friction ridges against the surface asperities of the countersurface. Skin deformation due to hysteresis increases with normal load and contact pressure [36, 38, 39]. The deformation term can be expressed as follow:

$$\mathrm{F_{f,def}} = \frac{3}{16}\beta\frac{\delta}{a}N \qquad (3)$$

In which β equals the viscoelastic hysteresis loss fraction, δ the indentation of the asperities into the skin, and a the contact radius [36]. For the contact mechanics of the fingertip, Hertz's theory can be used to describe the relation between the radius of curvature R, normal load N, and the deformation δ_H and contact radius a_H for a spherical contact:

$$a_H = \left(\frac{3}{4}\frac{RN}{E^*}\right)^{1/3} \qquad (4)$$

$$\delta_H = \left(\frac{9}{16}\frac{N^2}{RE^{*2}}\right)^{1/3} \qquad (5)$$

Where E^* equals the reduced elastic modulus, as a result of surfaces in contact [36]. Friction is often quantified by the *Coefficient of Friction* (COF), symbolized by the dimensionless value μ. The COF describes the relation between the measured $\mathrm{F_{f,tot}}$ and the applied normal load $\mathrm{F_N}$:

$$\mathrm{F_{f,tot}} = \mu \cdot \mathrm{F_N} \qquad (6)$$

The COF determines the required grip force to hold an object by hand safely. If friction is reduced, for instance, because oil has made the surface slippery, a higher grip force is necessary to hold the object. Therefore, the lower the COF, the higher the grip force must be. Under dry conditions, the adhesion at the skin-object interface and the deformation of the skin (and its sub-surface tissues) contribute to the COF [40]. Apart from adhesion and deformation, the contact conditions, as well as the moisture in between and the film thickness in relation to the surface texture of the surfaces in contact, influence the friction [41].

2.3. Skin Friction

The relationship between the surface texture and friction can be determined by different statistical surface roughness parameters, such as the arithmetic average roughness $\mathrm{R_a}$, the root mean square roughness $\mathrm{R_q}$ (or RMS) and the average peak-to-valley height roughness $\mathrm{R_z}$ [31, 37]. A surface texture with a larger $\mathrm{R_a}$ will usually result in higher friction. The surface roughness of the skin itself varies, depending on the section of the human body. The skin-surface roughness of the index finger typically lies between a $\mathrm{R_a}$ of 19-33 µm and $\mathrm{R_z}$ of 62-99 µm. A positive correlation between the number density of asperities at the fingertip and the COF has been observed for the skin-surface roughness [42]. Derler et al. [40] analysed the friction behaviour under dry contact conditions by rubbing the fingertip against glass surfaces which vary in surface roughness. They observed the highest COF of 2.25 ± 0.82 against a dry, smooth glass surface ($\mathrm{R_Z}$ = 0.05 ± 0.01 µm) for contact pressures of 20 ± 2 kPa, while a relatively low COF of only 0.63 ± 0.22 was observed for dry, rough glass ($\mathrm{R_Z}$ = 45.0 ± 5.6 µm). However, a rougher surface (up to R_q = 90) increased the COF by increasing object-surface roughness, due to the interlocking mechanism, which contributes to the overall friction. This leads to the overall conclusion that the COF between the fingertip skin and the countersurface, initially decreases with the increase in object-surface roughness (due to the adhesion term, characterised by the contact area), but then increases to a certain value (due to deformation term, characterised by hysteresis and interlocking mechanism) [39, 41].

3. DESIGN PRINCIPLES

3.1. Bio-Grasping Methods

When grasping an object, the contact mechanism is based on the interaction between two (or more) different types of surfaces. In order to improve the grip action, the following grasping methods should be discussed, Figure 3.1:

I. *Contact between two rigid surfaces*

Few contact points are in contact between two rigid surfaces. Therefore, friction is independent of the contact area. This is generally the case for commercialized prosthetic hands; a (rigid) object is held between the rigid contact surface(s) of the artificial finger. The grip between two rigid contacting surfaces can only be increased by increasing the normal force and the COF.

II. *Contact between one (or two) deformable surface(s)*

Friction is much larger due to the increase in the contact area as a result of the deformation of the surface under load. The deformable surface(s) leads to normal forces in various directions, which can increase the grip; a phenomenon in which the role of friction becomes less critical. This phenomenon can be found at the human fingertip.

III. *Shaping around an object*

The object is grasped by shaping around the object, which results in normal forces perpendicular to the shape of the object, thus increasing the grip strongly. In this case, the role of friction becomes less important. This phenomenon can be found not just when the hand shapes around on object, but also at the fingertip which comprises of soft skin-tissue that is able to adapt to a large variety of material properties.

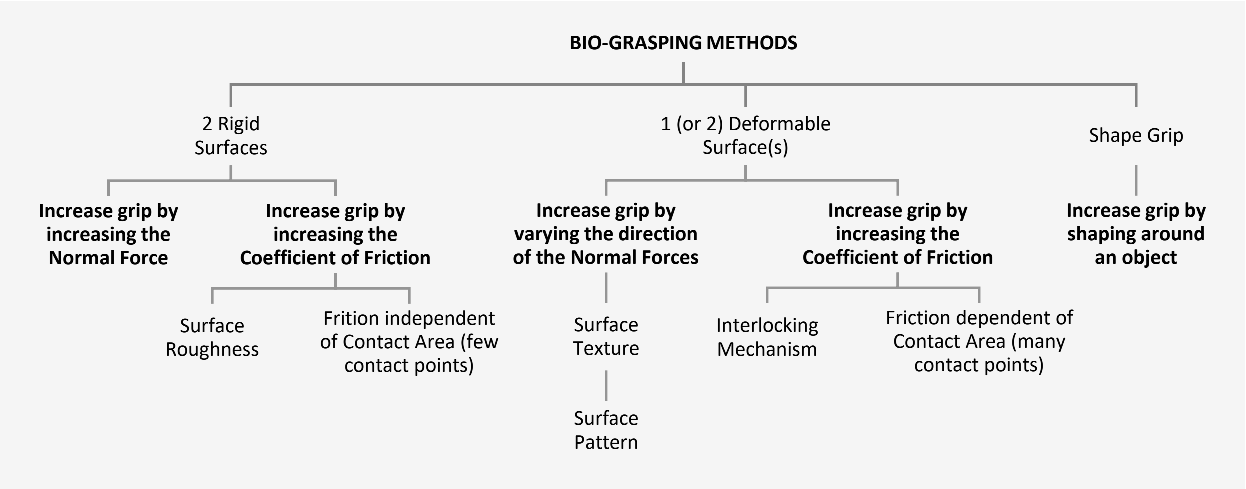

Figure 3.1. Biological Grasping methods based on the human finger

To summarize, when grasping an object, the grip can be increased:

a. by increasing the normal force;
b. by increasing the coefficient of friction;
c. by varying the direction of the normal forces (only in case of deformable contact surface(s));
d. by shaping around an object.

Note that the friction can be zero for option c. and d. while still having sufficient grip.

3.2. Bio-Principles of the Human Fingertip

Human fingertip-object manipulation is generally based on the contact mechanism between a (soft) deformable surface and a rigid object surface. In order to improve the grip action of prosthetic hands, the following fingertip skin-surface phenomena should be considered:

I. *Skin surface topography generate a larger (and increasing) contact area*

The biological topography at the fingertip generates a larger and increasing contact area under load. The friction ridges at the fingertip (with even smaller asperities) increase the contact point and generate additional interlocking effects under load, thus increasing the friction.

II. *Direction-dependent pattern deformation influence the grip force*

The skin along the friction ridges is locally stiffer than across the ridge and have been observed to slip earlier when aligned with the direction of motion [25]. In addition, it is believed that the grip increases perpendicular to each ridge. Therefore, the direction-dependent pattern deformation of the ridges at the fingertip influence the grip action; the grip increases in all direction due to the concentric pattern of the ridges.

III. *The soft fingertip is able to shape around an object, thereby increasing the grip.*

The human fingertip can be defined as a hybrid structure comprised of soft and hard components. The soft components allow safe interaction with surrounding objects due to their adaptability to the shape of the object, which increases the grip. In addition, the hard components are able to handle the weight of objects.

3.3. Bio-Principles of Adhesive Surfaces

The optimized biological adhesive surface structures of various animals are a result of combined strategies at different scale levels:

I. *Hierarchical structures are able to adapt to rough surfaces and distribute stress*

Biological adhesive structures found in gecko toe pads, spiders, and insects consist of hairy structures (setae). With the setae's ability to deform, hierarchical (micro/nano-) structures allow adaptability to rough surfaces and uniform distribution of stress.

II. *Gradients in mechanical properties influence the elastic modulus, and thus the surface’ attachment ability*

The elastic modulus is an essential parameter of structured biological adhesive. It has been observed that setae generally display gradients of mechanical properties. Setae are not only able to vary their material properties (e.g., by binding water molecules), but come in various shapes that influence the local stiffness (e.g., a narrowing diameter at the neck of the seta, allows the tip to bend thereby achieving better attachment to an uneven surface).

III. *Geometric (contact) parameters influence the adhesion*

The geometry of setae determines their adhesion abilities. Mushroom-like (or T-shaped) setae tips generate much higher adhesion on smooth surfaces, due to their geometry-induced homogenous stress distribution.

3.4. Conclusion

Biological (dry) adhesive surfaces generally consist of structures that are multi-scale, hierarchical and/or demonstrate mechanical gradient properties, which influence the elastic modulus. These contact mechanisms generally consist of deformable surface structure, which allows adaptability to rough surfaces and uniform distribution of stress. Although this behaviour also characterized the human fingertip, these contact mechanisms are generally not applicable for the rigid contact surfaces of commercialized prosthetic hands. Therefore, the contact mechanism between a deformable surface can be of interest in engineering a bio-inspired surface structure that can improve the grip action of prosthetic hands. Taken into account the fact that a low-cost 3D printing technology will be used during the experiment, the engineering of hierarchical (micro/nano-) structures and complex gradients in mechanical properties is not feasible. In this experimental study, the emphasis will be on analysing the frictional characteristics of soft, deformable surface patterns by systematically modifying topographical features at the surface.

4. DESIGN APPROACH

4.1. Design Requirements

The frictional characteristics of soft, deformable, 3D printed surface patterns will be analysed and evaluated, with the aim of providing a guideline for the engineering of bio-inspired surface with increased grip. The bio-inspired surface will be engineered with the idea of future integration with 3D printed prosthetic hands, such as the non-assembly 3D printed prosthetic presented by Cuellar et al. [4]. For this purpose, the 3D printed bio-inspired surface structure should meet the following requirements:

- Manufactured using 3D printing technology, i.e. the Fused Deposition Modeling (FDM) process;
- Based on design principles in nature (bio-inspired);
- Able to be integrated into a 3D printed hand prosthesis, i.e. instead of being an additional part, such as a glove.

4.2. Design Approach

The iterative design approach of the experimental study was based on a cyclic process of prototyping, testing, analysing, and refining the design. The experimental study can be roughly divided into two phases.

In phase one, the geometry of a single 3D printed surface feature were analysed by systematically modifying the height *h*, the thickness *d*, the wavelength λ, and curvature alignment α for a basic shape (D = d), Figure 4.1a. As discussed in Chapter 3, mushroom-like setae tips generate much higher adhesion on smooth surfaces. In addition, the narrowing diameter at the tip of setae allows for the tip to bend to achieve better attachment to a countersurface. Based on the design principles of bio-adhesives surface, an addition T-shaped (D > d) surface feature was introduced. The T-shaped features consist of an additional parameter; the tip thickness *D*, Figure 4.1b.

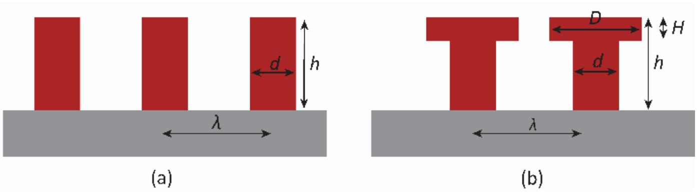

Figure 4.1. Front view of the soft, deformable 3D printed features (red) printed on top of a rigid surface (grey), with varying thickness d, height h and wavelength λ for a (a) basic shape D = d, and (b) T-shape D > d.

The topographical parameters were modified, tested and refined in the following order:

- Height (h);
- Thickness (d);
- Tip thickness (D);
- Wavelength λ; and
- Curvature alignment α

In phase two, these parameters were combined into different patterns for optimal surface friction, using the experimental results from phase one as a guideline. The 3D printed surface features (Figure 4.1, red) were printed on an underlying, rigid surface (Figure 4.1, grey), thereby disregarding the effects of the deformation of the underlying structure on the friction properties. The underlying, rigid surface was 20 mm wide and 34 mm long, to mimic the surface area of a thumb, and 4 mm thick, Figure 4.2.

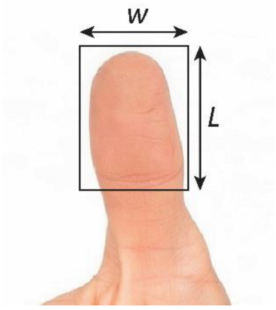

Figure 4.2. The surface area of the thumb used for the underlying, rigid surface, which will be 20 mm wide, 34 long, and 4 mm thick.

4.3. FDM 3D Printing technology

Additive Manufacture (AM), generally referred to as 3D printing, is based on a digital computer-aided design (CAD) model. AM is a process in which a 3D part is built in a layer-by-layer fashion. Within AM, there are several different types of printing techniques, that vary in layer application and bonding, but consist of similar process steps. The main principle is to slice the 3D digital model into small cross-sections, thereby creating a Stereolithography (.STL) file. The STL file is compatible to send to a 3D printer for extrusions, Figure 4.3.

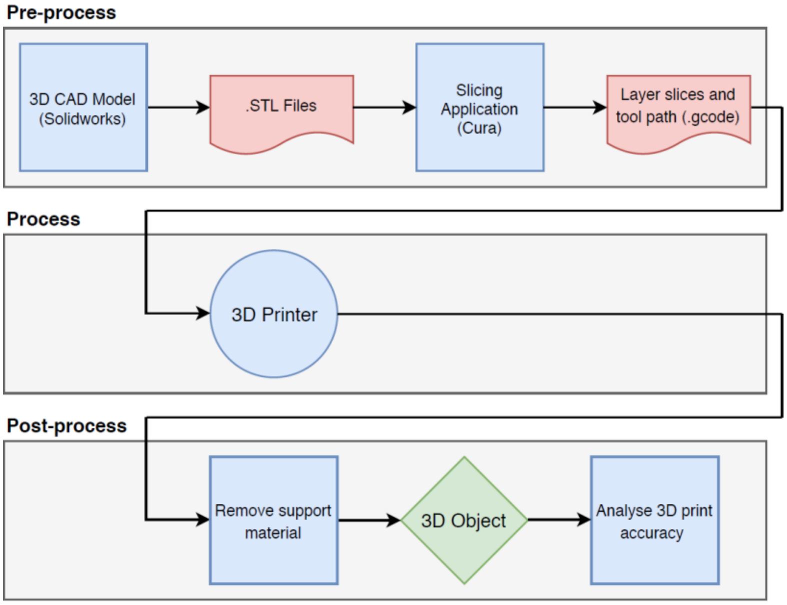

Figure 4.3. Workflow 3D printing

The most common 3D printing technology is the Fused Deposition Modeling (FDM) process. FDM uses a filament of thermoplastic material that is heated and then pushed through a nozzle in which the 3D part is built layer-by-layer. FDM 3D printing technology has many advantages, such as cost-effectiveness, range of materials, ability to produce complex shapes, print speeds, and accessibility. However, there are some disadvantages, such as the limitation in build size, support material, inaccuracy in small dimension printing, and temperature fluctuations. In this experimental study, the FDM 3D printer, Ultimaker 3, was used. The Ultimaker 3 comprises of two print nozzles, both with a diameter of 0.4 mm. The two print cores of Ultimaker 3 makes it possible to print with two different materials [43].

4.4. FDM 3D Printing Material

Various parameters should be considered when choosing an AM technique, such as the layer thickness, available material and their properties, and the possibility to print multiple materials. However, this choice is limited by the availability and accessibility of 3D printers. Choosing the right material is critical to the success of any 3D printed part. However, the selection of available materials depends on the chosen 3D printer. The following materials are available for the Ultimaker 3: Polylactic acid (PLA), Tough PLA, acrylonitrile butadiene styrene ABS, Nylon, co-polyester (CPE), CPE+, polycarbonate (PC), polypropylene (PP), thermoplastic polyurethane (TPU) 95A, and the additional support material polyvinyl alcohol (PVA). The materials nylon, PP, and TPU 95A are considered (semi-)flexible material, Table 4.1.

Table 4.1. Young's Modulus and Yield Strength of (semi-)flexible materials of the Ultimaker 3 FDM Printer [43].

	Young's Modulus (MPa)	**Yield Strength (MPa)**
Nylon	579	27.8
PP	220	8.7
TPU 95A	26	8.6

Materials with a low stiffness (young's modulus) are more adaptable to rough surfaces, when loads are applied. However, there are some obvious disadvantages for low-modulus materials, such as the tendency to creep. TPU 95A is a material that is both flexible and strong, which can withstand high impacts without plastic deformation and resist normal wear. Therefore, the flexible filament TPU 95A was used in this experimental study [43].

5. CONCEPTUAL DESIGN: SINGLE VARIABLE

5.1. Initial 3D FDM Print Conditions for TPU 95A (Spool A)

Thermoplastic polyurethane (TPU) 95A is a flexible, abrasion-resistant thermoplastic. Due to its elastic properties, the material is more difficult to print compared to stiffer thermoplastic [43]. Initial 3D printing, using the default settings of Ultimaker 3, resulted in low accuracy for small dimension printing with TPU. This was especially the case for 3D printed pillars with a diameter of less than 0.8 mm. The smallest nozzle diameter of 0.4 mm, of the Ultimaker 3, should, in theory, be able to print a minimal diameter of 0.4 mm. However, printing this small size was a challenge using TPU. The material is sensitive to the print speed due to its elastic properties. The elastic properties of TPU can result in the compression of the material, jamming of the material in the print head of the 3D printer, holes or gaps in the layers, and strings of material between parts of the original design, Figure 5.1. After initial testing, the optimal print speed for small 3D printed features using TPU was set on 15 mm/s. Lowering the print speed resulted in the 3D printer's ability to print a minimal pillar diameter of 0.5 mm (compared to the initial 0.8 mm). More information about the printer settings, can be found in Appendix A.

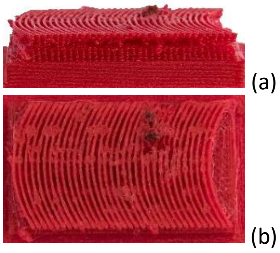

Figure 5.1. A 3D printed test sample for the Ultimaker's default print speed of 25 mm/s: (a) side view of the layers that are not properly bonded on top of each other, (b) top view in which extra material between the lines and some burnt clumping material can be observed.

5.2. Geometric Features: Height (h)

The smallest printable pillar diameter was set on 0.5 mm, for a print speed of 15 mm/s. The pillar height h on the friction properties was analysed for the parameters h_1 = 0.4 mm, h_2 = 0.8 mm and h_3 = 1.2 mm. The thickness d and wavelength λ were kept constant, with a value of 0.5 mm and 1.6 mm, respectively. The 3D CAD Models d00001, d00002, and d00003 consisted of 21 rows of 12 pillars each, which resulted in a total of 252 pillars, Figure 5.2.

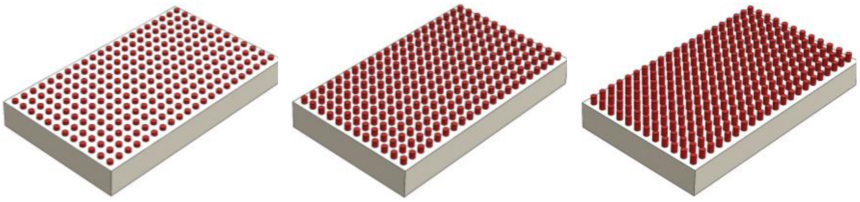

Model Nr.	d00001	d00002	d00003
d [mm]	0.5	0.5	0.5
h [mm]	h_1	h_2	h_3
λ [mm]	1.6	1.6	1.6

Figure 5.2. Geometric features for basic shaped pillars (D = d), with variable height h_1 = 0.4 mm, h_2 = 0.8 mm, h_3 = 1.2 mm. The 3D CAD model consisted of a total amount of 252 pillar (21 rows of 12 pillar).

The 3D printed features, shown in Figure 5.3, demonstrate a low accuracy for small dimension printing. The relatively small pillar height *h* resulted in features that were not clearly distinguished from another and did not display any deformation. In addition, a wavelength *λ* of 1.2 mm resulted in the fusion of the 3D printed features. Due to the low printing accuracy and the high discrepancy between the 3D printed features, the printed model numbers d00001, d00002 and d00003 are excluded for further testing of their surface friction properties.

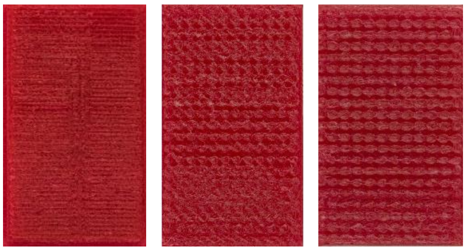

Model Nr.	d00001	d00002	d00003
h [mm]	h_1	h_2	h_3

Figure 5.3. Top view of the 3D printed features for basic shaped pillars (D = d) with variable pillar height h_1 = 0.4 mm, h_2 = 0.8 mm, h_3 = 1.2 mm.

The following recommendations were used for further 3D printing: first, the benchmark for the pillar height *h* was set to 4 mm at which deformation of the pillar can be clearly observed; second, the wavelength *λ* between the pillars was increased to prevent fusion of the 3D printed features due to printing inaccuracy; and finally, the 3D printing of lines were introduced to analyse whether or not 3D printed lines resulted in more accurate printing compared to 3D printed pillars.

5.3. Geometric Features: Thickness (d)

The role of the thickness d on the friction properties was analysed for basic shaped (D = d) pillars and lines, Figure 4.1. The thickness *d* was systematically modified and analysed for the parameters d_1 = 0.5 mm, d_2 = 0.8 mm and d_3 = 1.2 mm. The height *h* and wavelength *λ* were kept constant, with a value of 4.0 mm and 2.8 mm, respectively, Figure 5.4.

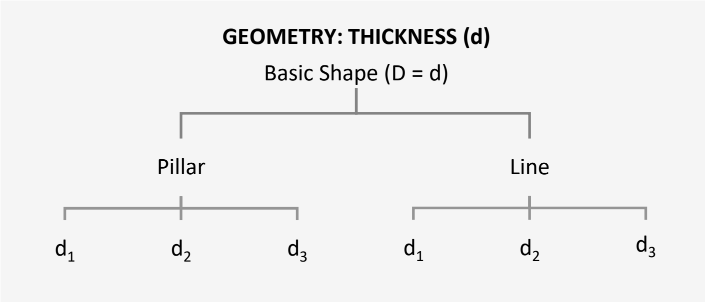

Figure 5.4. Geometric features with variable thickness d_1 = 0.5 mm, d_2 = 0.8 mm and d_3 = 1.2 mm.

The 3D CAD Models d00101, d00111 and d00121 consisted of 12 rows of 7 pillars each, which resulted in a total of 84 pillars. The 3D CAD Models d00201, d00211 and d00221 consisted of 12 rows of straight lines, Figure 5.5.

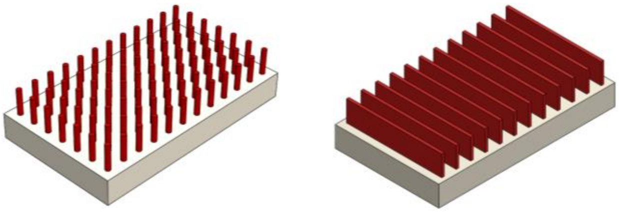

Model Nr.	**d00101**	**d00111**	**d00121**	**d00201**	**d00211**	**d00221**
d [mm]	d_1	d_2	d_3	d_1	d_2	d_3
h [mm]	4.0	4.0	4.0	4.0	4.0	4.0
λ [mm]	2.8	2.8	2.8	2.8	2.8	2.8

Figure 5.5. The geometric features of basic shaped (D = d) pillars (d00101, d00111, d00121) and lines (d00201, d00211, d00221), with variable thickness d_1 = 0.5 mm, d_2 = 0.8 mm and d_3 = 1.2 mm.

The 3D printed features, shown in Figure 5.6, display a high discrepancy in printing accuracy between the 3D printed pillars, especially for small dimension printing. In addition, it is observed that the direction of the print head influences the shape of the pillars. This might be the result of the still heated flexible TPU when moving the print head from one pillar to the next.

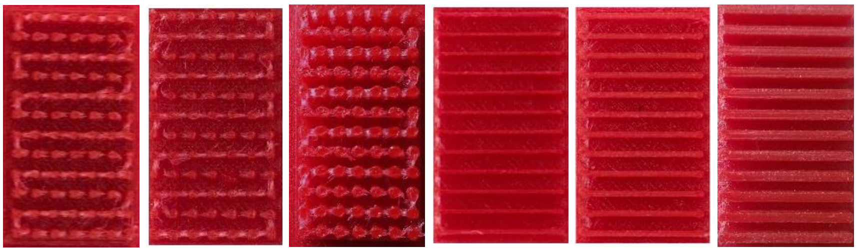

Model Nr.	**d00101**	**d00111**	**d00121**	**d00201**	**d00211**	**d00221**
d [mm]	d_1	d_2	d_3	d_1	d_2	d_3

Figure 5.6. Top view of the 3D printed geometric features of basic shaped (D = d) pillars (d00101, d00111, d00121) and lines (d00201, d00211, d00221), with variable thickness d_1 = 0.5 mm, d_2 = 0.8 mm and d_3 = 1.2 mm.

5.4. Tip Geometry: Thickness (D, d)

The tip thickness *D* on the friction properties was analysed for T-shaped (D > d) pillars and lines, Figure 4.1. The thickness *d* and *D* was systematically modified and analysed for the parameters d_1 = 0.5 mm, d_2 = 0.8 mm, D_1 = 1.6 mm and D_2 = 2.4 mm. The height *h* and wavelength *λ* were kept constant, with a value of 4.0 mm and 2.8 mm, respectively, Figure 5.7.

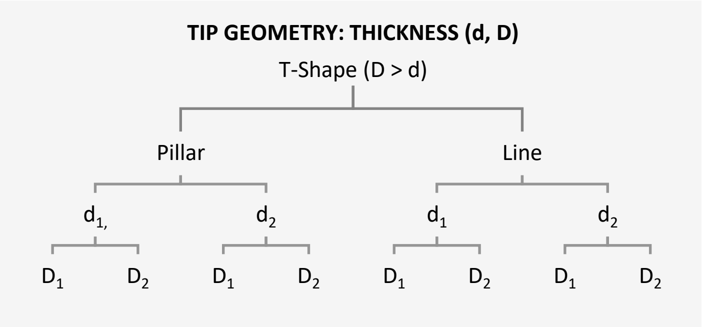

Figure 5.7. Tip geometry with variable thickness d_1 = 0.5 mm, d_2 = 0.8 mm, D_1 = 1.6 mm and D_2 = 2.4 mm.

The 3D CAD Models d00102, d00112, d00103 and d00113 consisted of 12 rows of 7 pillars each, which resulted in a total of 84 T-shaped pillars. The 3D CAD Models d00202, d00212, d00203 and d00213 consist of consisted of 12 rows of T-shaped lines, Figure 5.8.

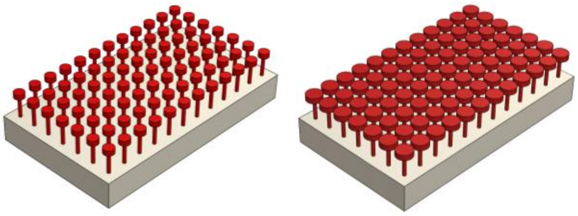

Model Nr.	**d00102**	**d00112**	**d00103**	**d00113**
d [mm]	d_1 / D_1	d_2 / D_1	d_1 / D_2	d_2 / D_2
h [mm]	4.0h / 0.8H	4.0h / 0.8H	4.0h / 0.8H	4.0h / 0.8H
λ [mm]	2.8	2.8	2.8	2.8

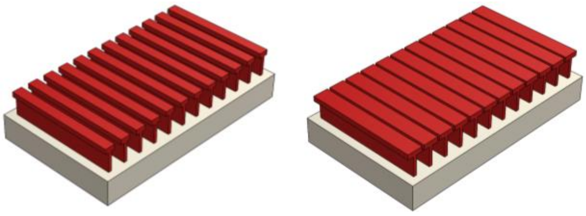

Model Nr.	**d00202**	**d00212**	**d00203**	**d00213**
d [mm]	d_1 / D_1	d_2 / D_1	d_1 / D_2	d_2 / D_2
h [mm]	4.0h / 0.8H	4.0h / 0.8H	4.0h / 0.8H	4.0h / 0.8H
λ [mm]	2.8	2.8	2.8	2.8

Figure 5.8. The tip geometry of T-shaped (D > d) pillars (d00102, d00112, d00103 and d00113) and lines (d00202, d00212, d00203 and d00213), with variable thickness d_1 = 0.5 mm, d_2 = 0.8 mm, D_1 = 1.6 mm and D_2 = 2.4 mm.

The 3D printed features of the tip geometry, shown in Figure 5.9, displayed similar results compared to Figure 5.6. Again, a high discrepancy was observed between the 3D printed pillars. This discrepancy was especially observed for the 3D printed pillars d00103 and d00113, with tip thickness D_2. The increasing ratio between *d* and *D* resulted in a decrease in print accuracy of the tip (*D*) on top of the pillar (*d*), Figure 5.9.

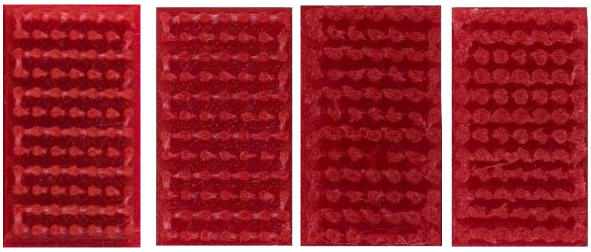

Model Nr.	d00102	d00112	d00103	d00113
d [mm]	d_1 / D_1	d_2 / D_1	d_1 / D_2	d_2 / D_2

Model Nr.	d00202	d00212	d00203	d00213
d [mm]	d_1 / D_1	d_2 / D_1	d_1 / D_2	d_2 / D_2

Figure 5.9. Top view of the 3D printed features of the tip geometry of T-shaped pillars (D > d) pillars (d00102, d00112, d00103 and d00113) and lines (d00202, d00212, d00203 and d00213), with variable thickness $d_1 = 0.5$ mm, $d_2 = 0.8$ mm, $D_1 = 1.6$ mm and $D_2 = 2.4$ mm.

In addition, it was observed that the 3D printed pillars were quite fragile compared to the 3D printed lines of similar thickness, which resulted in the breaking of the pillars during the friction test. Although it was possible to increase the thickness of the pillars, this would result in far less deformation. The following findings were proposed for further 3D printing: first, the thickness *d* was set on the smallest printing thickness of 0.5 mm in order to further test their deformability; second, due to the high discrepancy and fragility of the 3D printed pillar, for the next step the focus was set on the printing of lines instead of pillars.

5.5. Surface Features: Wavelength (λ)

The initial wavelength λ was set on 2.8 mm for the previous samples. The role of the wavelength λ on the friction properties was analysed next for the parameters $\lambda_1 = 2.8$ mm, $\lambda_2 = 1.8$ mm, $\lambda_3 = 0.8$ mm. The thickness *d* and height *h* were kept constant, with a value of 0.5 mm and 4.0 mm, respectively. The 3D CAD Models d00201, d00221, and d00231 consisted of a total of 12, 18 and, 21 lines, respectively, Figure 5.10.

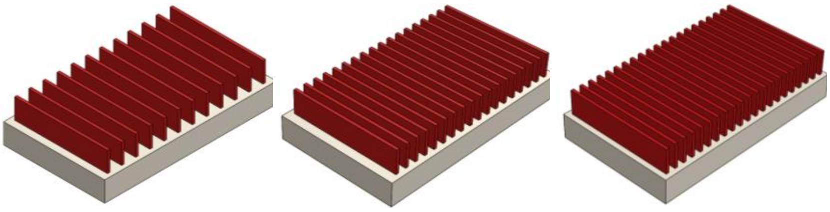

Model Nr.	d00201	d00221	d00231
d [mm]	0.5	0.5	0.5
h [mm]	4.0	4.0	4.0
λ [mm]	λ_1	λ_2	λ_3

Figure 5.10. The surface features with variable wavelength λ_1 = 2.8 mm, λ_2 = 1.8 mm and λ_3 = 0.8 mm.

The 3D printed features, shown in Figure 5.11, displayed no real discrepancy between the 3D printed lines. However, as mentioned before, the direction of the print head affects the printed features. When the print head goes from one line to the next, it leaves some additional material between these lines. Therefore, the lines at one end were connected to each other, resulting in the stiffening of the structure on one side (see the left side on each image in Figure 5.11).

Model Nr.	d00201	d00221	d00231
λ [mm]	λ_1	λ_2	λ_3

Figure 5.11. Top view of the 3D printed surface features with variable wavelength λ_1 = 2.8 mm, λ_2 = 1.8 mm and λ_3 = 0.8 mm.

To test the role of the wavelength λ on the friction properties, without the additional material between the lines interfering with the results, the material in-between was removed manually after printing.

5.6. Surface Features: Curvature (α)

The role of the angle *α* of a curvature on the friction properties was analysed for the parameters α_1 = 0°, α_2 = 68° with an inner radius of 16 mm and α_3 = 124° with an inner radius of 10 mm. The thickness *d*, height *h* and wavelength λ were kept constant, with a value of 0.5 mm, 4.0 mm and 1.8 mm, respectively. Note that, due to the results which will be discussed in Chapter 7, the wavelength was set on an optimal distance of 1.8 mm. The 3D CAD models d00221, d00302 and d00303 consisted of a total of 18, 17 and 16 lines, respectively, Figure 5.12.

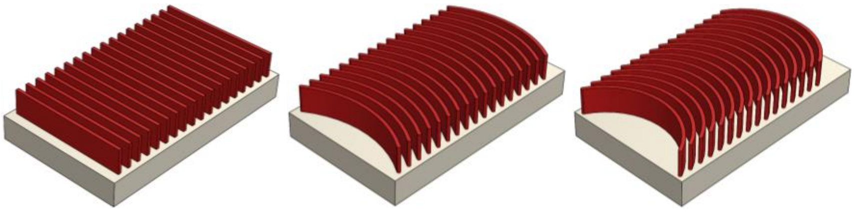

Model Nr.	d00221	d00302	d00303
d [mm]	0.5	0.5	0.5
h [mm]	4.0	4.0	4.0
λ [mm]	1.8	1.8	1.8
α [°]	α_1	α_2	α_3

Figure 5.12. The surface features with variable angle $\alpha_1 = 0°$, $\alpha_2 = 68°$ with an inner radius of 16 mm, and $\alpha_3 = 124°$ with an inner radius of 10 mm.

As mentioned before, the direction of the print head affects the printed features. Again, this was the case for models d00302 and d00303, where additional drops of material were found between the lines, Figure 5.13. Changing the placement at the build plate, the print speed and print temperature of the printer did not change this phenomenon. However, increasing the wavelength minimalized the additional material between the lines.

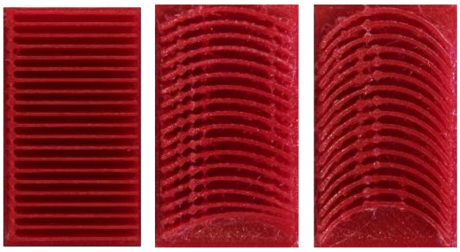

Model Nr.	d00221	d00302	d00303
λ [mm]	α_1	α_2	α_3

Figure 5.13. Top view of the 3D printed surface features with variable angle $\alpha_1 = 0°$, $\alpha_2 = 68°$ with an inner radius of 16 mm and $\alpha_3 = 124°$ with an inner radius of 10 mm.

6. EXPERIMENTAL SETUP

6.1. Theoretical Background: Coefficient of Static Friction μ_s

3D printed surface features were printed on top of a rigid surface and consisted of pillars or lines varied in thickness *d*, tip thickness *D,* wavelength λ, and curvature alignment α. These topographical parameters were systematically modifying to analyse the frictional characteristic of the soft, deformable 3D printed patterns on top of a rigid surface. As mentioned before, the friction force is defined as the resistance force between two surfaces in relative motion. (Dry) Friction can be divided into static friction force F_s and dynamic (or kinetic) friction force F_k. The F_s holds the surfaces in contact in a stationary static position until the maximum static friction force F_s (max) is reached and the surfaces start to move relative to each other, transitioning into F_k.

$$F_s \text{ (max)} > F_s \qquad (7)$$

Friction is often quantified by the COF, symbolized by the dimensionless value μ. The coefficient of static friction μ_s is generally higher compared to its kinetic counterpart. The F_s is considered to be the result of the forming junctions between the deformable surface features, i.e. the asperities of both surfaces. The dimensionless value μ_s is the ratio of the F_s (max) between two surfaces before sliding, and the normal force F_N perpendicular to the surface [44].

$$\mu_s = F_s \text{ (max)} / F_N \qquad (8)$$

The 3D printed surface patterns are engineered with the idea of future integration with 3D printed prosthetic hands to increase the grip during object manipulation. When holding an object between the fingertips of the prosthetic hands, the contact mechanism is in a stationary static position in which μ_s is considered to be the result of the forming junctions between the deformable surface features. Therefore, the frictional characteristics of the soft, deformable 3D printed patterns were assessed by measuring μ_s.

6.2. Test Setup

The experimental set up was composed of: (1) a 3D printed test sample (red); (2) a 3D printed container with (x) weight on top; (3) a frictionless pulley; (4) a loading container with mass m_2; (5) a 3D printed support-table; and (6) a testing countersurface, Figure 6.1. The weight of the 3D printed test sample (4 g), the 3D printed container (56 g) and (x) weight on top combined, form the mass m_1.

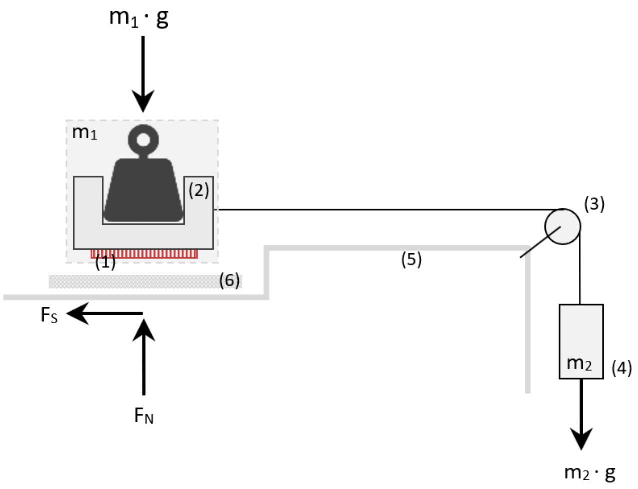

Figure 6.1. Schematic sketch of the experimental set up for static coefficient of friction μ_s evaluation. (1) a 3D printed test sample (red); (2) a 3D printed container with (x) weight on top; (3) a frictionless pulley; (4) a loading container with mass m_2; (5) a 3D printed support table; and (6) a testing countersurface. The weight of the 3D printed test sample (4 g), the 3D printed container (56 g) and (x) weight on top combined, form the combined mass m_1.

The 3D printed support-table, on which the frictionless pulley was attached, was placed on a table. A cable attached to the back of the 3D printed support-table was tied to the table to keep the test setup in position, Figure 6.2. Next, the glass countersurface was glued on top of the support-table. During the friction test, three different countersurface were tested, i.e. glass and two different sandpapers. The sandpapers were fixed on top of the glass countersurface using double-sided tape. Next, the 3D printed container, in which the 3D printed sample (Figure 6.1, red) was clamped, is placed on top of the countersurface. For each countersurface, different weights were placed on top of the 3D printed container, to simulate different F_N.

$$F_N = m_1 \cdot g \qquad (9)$$

A pulley cable was placed over the frictionless pulley. The pulley cable was attached to the 3D printed container (Figure 6.1, nr. 2) and the loading container (Figure 6.1, nr. 4). Different weight discs m_2 between 5 grams (smallest weight disc) and 1 kg (biggest weight disc), were placed in the loading container. The static friction force F_s holds the 3D printed sample in a stationary static position up to the point that it starts to slide, by adding m_2 in the loading container. The F_s is equal to $m_2 \cdot g$, until the maximum static friction force F_s (max) is reached, Figure 6.2.

$$F_s\ (\text{max}) = m_2 \cdot g \qquad (10)$$

Note that slip can be defined as the opposite of friction. Therefore, a higher μ indicates a lower slip factor [44]. The input for this model were:

- The combined mass, m_1 [kg];
- The loading container, m_2 [kg];
- Gravitational acceleration, g [m/s^2];
- Three different countersurface: glass, sandpaper P600 and sandpaper P240;

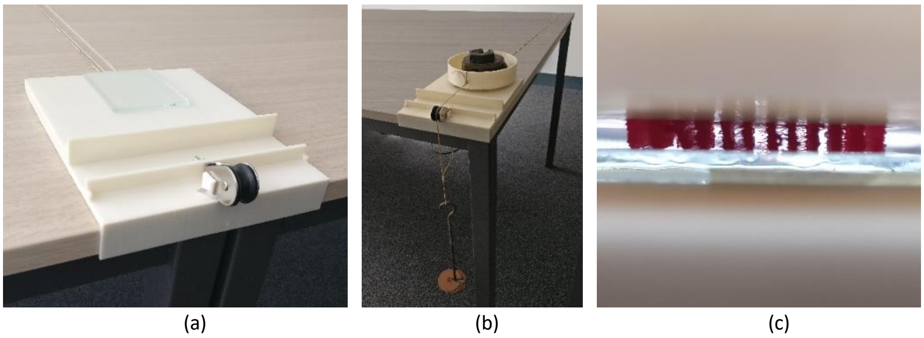

(a) (b) (c)

Figure 6.2. The experimental set up: (a) the 3D printed support-table with the glass countersurface on top, (b) the 3D printed test sample under load F_N, (c) a side view of the 3D printed test sample on top of the glass countersurface.

6.3. Test Equipment

The 3D printed PLA support-table consisted of a length and width of 180 mm and 150 mm (Figure 6.3, grey). Note that a trade-off was made between the width of the 3D printed container and the minimal length needed to slide against the countersurface, the maximum build volume of the Ultimaker 3, and the production time. The support-table consisted of a stop block (Figure 6.3, blue) and a connecting piece on which the pulley is mounted (Figure 6.3, yellow). The glass countersurface was glued onto the support table. The 3D printed PLA container (Figure 6.3, black) with an inner radius of 118 mm and thickness of 2.0 mm, suitable for the 1 kg weight disc of similar diameter, was placed on top of the countersurface. The 3D printed container was designed with a rectangular opening into which the 3D printed sample could be clamped, Figure 6.3. Detailed drawings of the 3D printed equipment can be found in Appendix B.

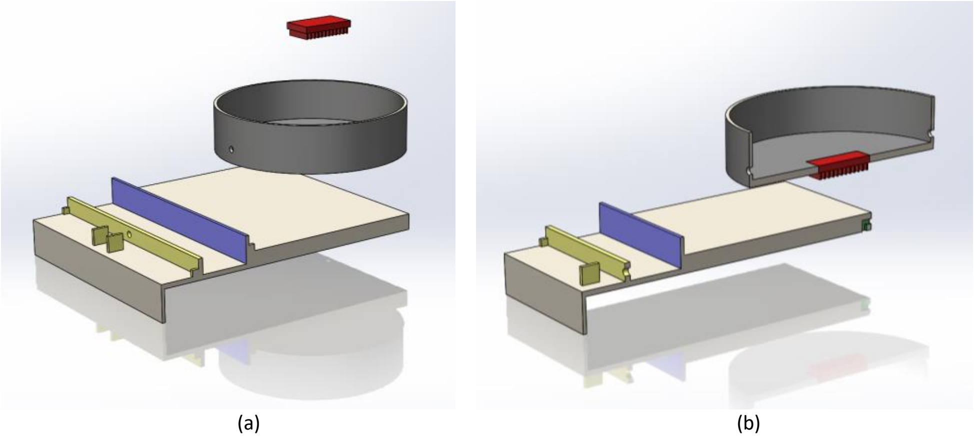

(a) (b)

Figure 6.3. Overview of the 3D printed equipment, redirected from top to bottom: the test sample (red); the container (black); the support-table (grey) with a stop block (blue), a connecting piece on which the pulley is mounted (yellow), and a hook on which a cable was attached (green). The latter was attached to the back of the 3D printed support-table and tied to a table to keep the test setup in position. (a) full view, (b) cross-section view.

6.4. Test Procedure

Each 3D printed sample was tested for nine different test scenarios, i.e. three different loads F_N and three different countersurfaces. A total of 25 test samples were tested three times for every nine different test scenarios, resulting in a total amount of 675 tests performed. The 3D printed surface features were designed with the idea of future integration of such a sample into the non-assembly 3D printed hand prosthesis presented by Cuellar et al. [4]. Three different normal forces were used, i.e. 3, 8, and 15N, within the pinch force range of the 3D printed hand prosthesis. Three different countersurfaces were used, i.e. glass (smooth), sandpaper P600 (fine) with an average particle diameter of 25.8 µm, and sandpaper P240 (rough) with an average particle diameter of 58.5 µm. With each new test, the sandpaper was renewed to prevent the wear of the asperities of the sandpaper from interfering with the results. After completing all the friction test cycles, the test was repeated again for three previous test samples. No significant difference could be observed between the two scenarios. Therefore, the assumption is that the wear of the 3D printed samples between each test could be neglected.

7. EXPERIMENTAL RESULTS: SINGLE VARIABLE

7.1. Geometric Features: Thickness (d)

The role of the thickness *d* on the friction properties was analysed for the parameters d_1 = 0.5 mm, d_2 = 0.8 mm and d_3 = 1.2 mm. The height *h* and wavelength λ were kept constant, with a value of 4.0 mm and 2.8 mm, respectively, Figure 5.5. The maximum static friction force F_S (max) and the average coefficient of static friction μ_S were measured for basic shaped pillars (blue) of the 3D CAD models d00101, d00111, and d00121, and for basic shaped lines (red) of the 3D CAD Models d00201, d00211 and d00221, Figure 7.1.

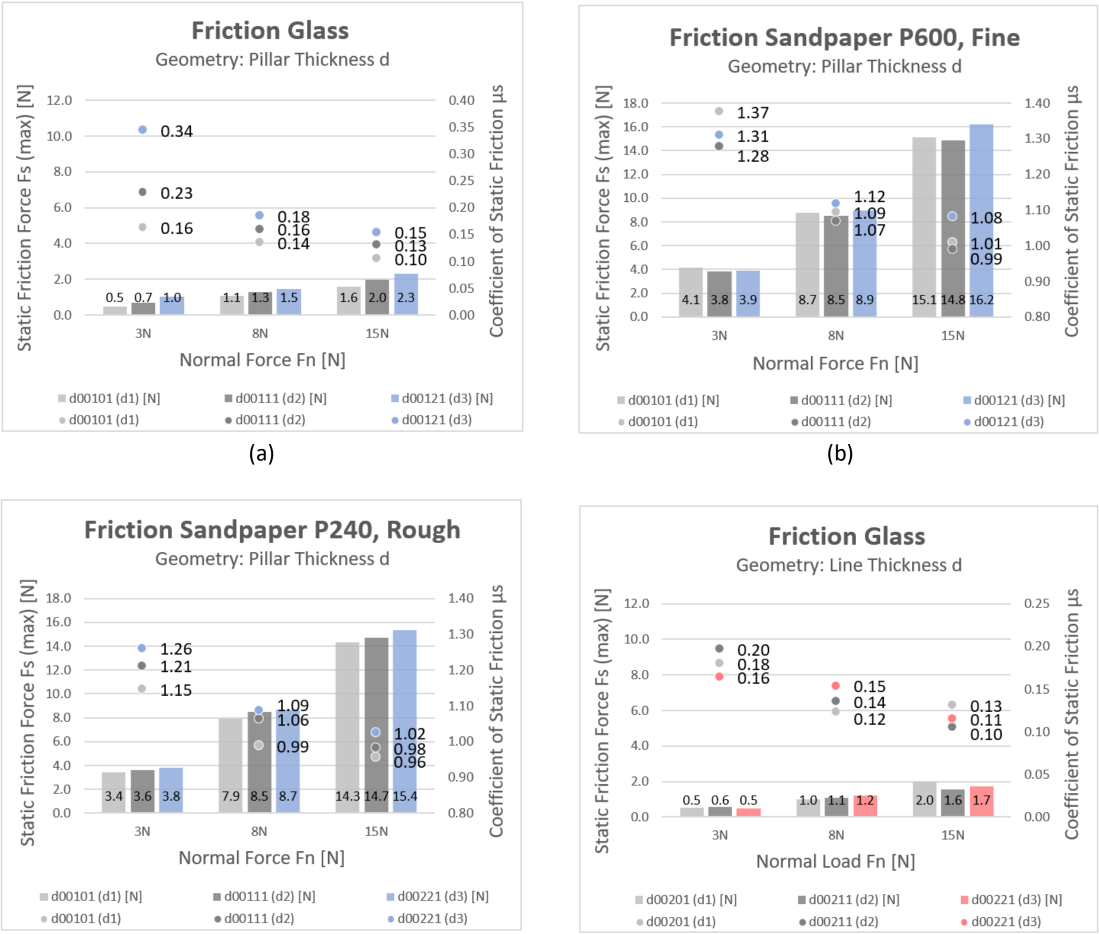

(a) (b)

(c) (d)

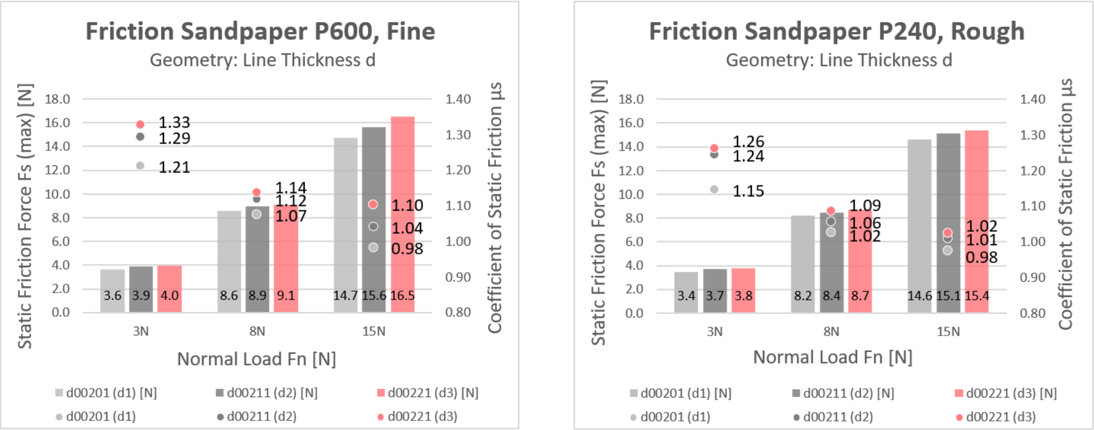

(e) (f)

Figure 7.1. The maximum static friction force F_s (max) [N] and coefficient of static friction μ_s of 3D printed pillars (a-c, blue) and lines (e-f, red), with variable thickness d_1 = 0.5 mm, d_2 = 0.8 mm and d_3 = 1.2 mm, for the countersurface glass (smooth), sandpaper P600 (fine), and sandpaper P240 (rough). The measured F_s (max) is represented by columns and the corresponding μ_s is represented by dots.

An increase in the μ_s was observed for increasing thickness *d*. However, as shown in Figure 7.1b, a slightly higher μ_s was displayed for the smallest pillar thickness. It is plausible that the higher μ_s for the smallest pillar thickness, is the result of an additional interlocking mechanism between the small deformable pillars and the fine sandpaper P600. In addition, an increased flattening of the 3D printed features was observed under increasing normal load F_n, thereby stiffening the overall surface structure, Figure 7.2.

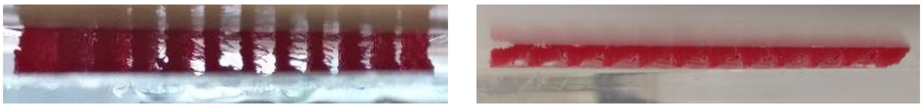

(a) (b)

Figure 7.2. Deformation of the 3D CAD model d00102 with the smallest pillar thickness d_1, under various normal load: (a) 3N and (b) 15 N.

7.2. Tip Geometry: Thickness (D, d)

The role of the tip thickness *D* on the friction properties was analysed for the parameters d_1 = 0.5 mm, d_2 = 0.8 mm, D_1 = 1.6 mm and D_2 = 2.4 mm. The height *h* and wavelength *λ* were kept constant, with a value of 4.0 mm and 2.8 mm, respectively, Figure 5.8. The F_s (max) and μ_s were measured for T-shaped pillars (blue) of the 3D CAD models d00102, d00112, d00103, and d00113, and for T-shaped lines (red) of the 3D CAD models d00202, d00212, d00203 and d00213, Figure 7.3.

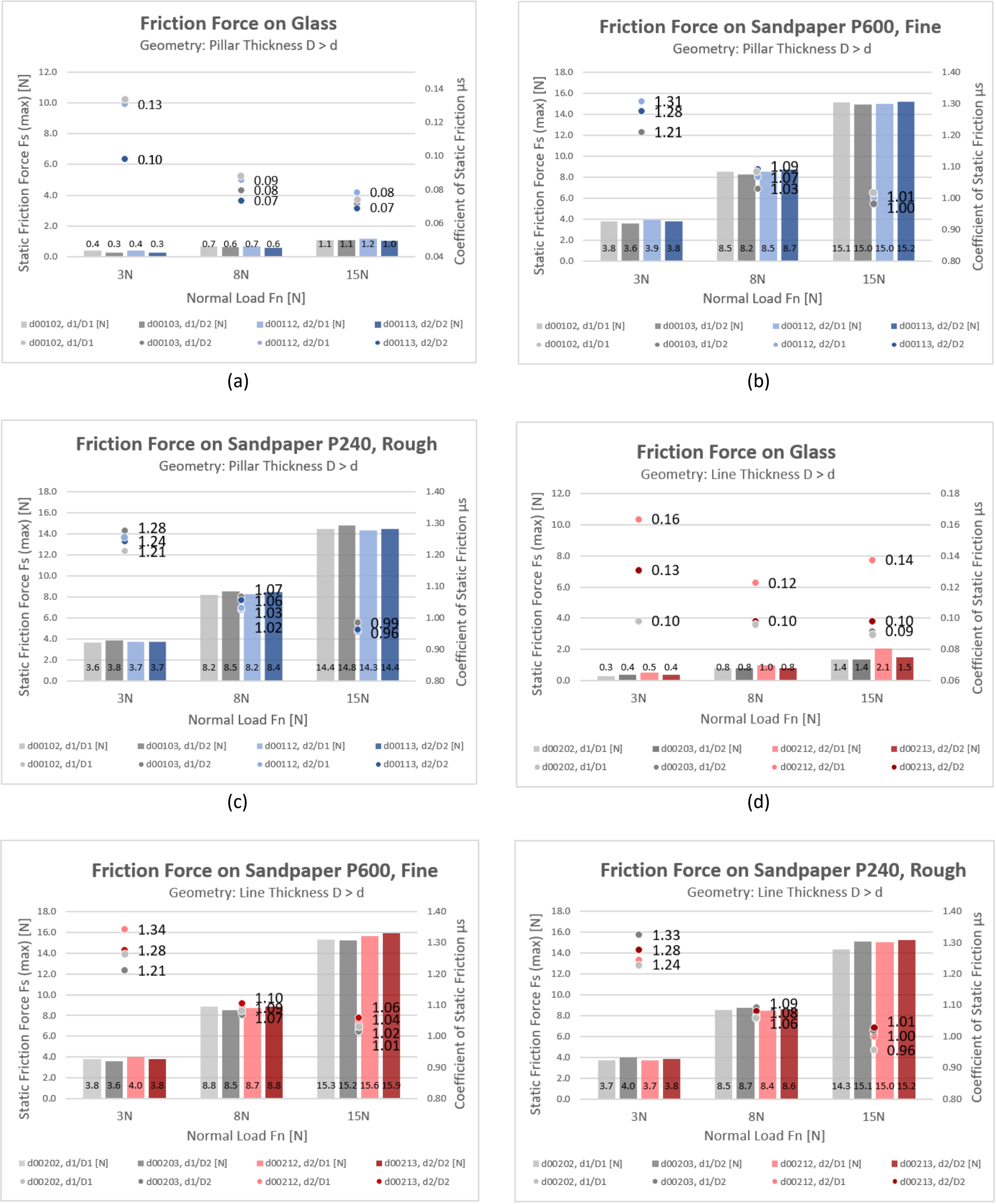

(a) (b) (c) (d) (e) (f)

Figure 7.3. The maximum static friction force F_s (max) [N] and coefficient of static friction μ_s of 3D printed pillars (a-c, blue) and lines (e-f, red), with variable thickness d_1 = 0.5 mm, d_2 = 0.8 mm, D_1 = 1.6 mm and D_2 = 2.4 mm, for the countersurface glass (smooth), sandpaper P600 (fine), and sandpaper P240 (rough). The measured F_s (max) is represented by columns and the corresponding μ_s is represented by dots.

As discussed in Chapter 2, the F_s is proportional to the real contact area. Therefore, the hypothesis was that an increase in F_s would be observed for increasing tip thickness *D*. Due to the T-shape, however, the surface friction is determined by the deformation of the stem (influenced by thickness d) and the contact area (influenced by the tip geometry D). The printed features d_2/ D_2 (i.e., less deformation, higher tip thickness) resulted in less flattening under similar load compared to d_1/ D_1, Figure 7.4. The bigger tip thickness D_2, was observed to generate a slightly higher μ_s compared to its D_1 counterpart, against the rough P240 sandpaper countersurface. This was not the case for the glass and P600 countersurface. It is plausible that the bigger thickness D_2, when bent, resulted in less real contact area against the glass countersurface, and less interlocking with the P600 countersurface, compared to its D_1 counterpart.

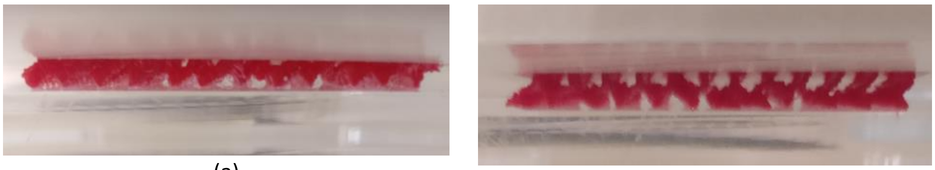

(a)

(b)

Figure 7.4. Deformation of the T-shapes lines of the3D CAD model: (a) d00202 d_1/D_1 and (b) d00213 d_2/D_2.

7.3. Surface Features: Wavelength (λ)

An increase in μ_s was observed for increasing thickness d, paragraph 7.1. However, this led to more stiffening of the 3D printed features. It was decided to maintain thickness d_1 in the following step to more clearly analyse the role of direction-dependent pattern deformation on the friction properties. The role of the wavelength λ on the friction properties was analysed for the parameters λ_1 = 2.8 mm, λ_2 = 1.8 mm, λ_3 = 0.8 mm. The thickness d and height h were kept constant, with a value of 0.5 mm and 4.0 mm, respectively, Figure 5.10. The F_s (max) and μ_s were measured for the 3D CAD models d00201, d00211, and d00231, Figure 7.5.

(a)

(b)

(c)

Figure 7.5. The maximum static friction force F_s (max) [N] and coefficient of static friction μ_s of 3D printed lines, with variable wavelength λ_1 = 2.8 mm, λ_2 = 1.8 mm and λ_3 = 0.8 mm, for the countersurface glass (smooth), sandpaper P600 (fine), and sandpaper P240 (rough). The measured F_s (max) is represented by columns and the corresponding μ_s is represented by dots.

As shown in Figure 7.5, the wavelength λ_2 of 1.8 mm generally displayed the highest resulting μ_s. The density of the printed features per mm^2 varied for samples d00201 (n_1 = 12 lines), d00221 (n_2 = 18 lines), d00231 (n_3 = 21 lines). To analyse the role of only the wavelength λ on μ_s a correction value was applied. This resulted in a correction factor of n_1/n_2 for sample d00221 and n_1/n_3 for sample d00231, Figure 7.6.

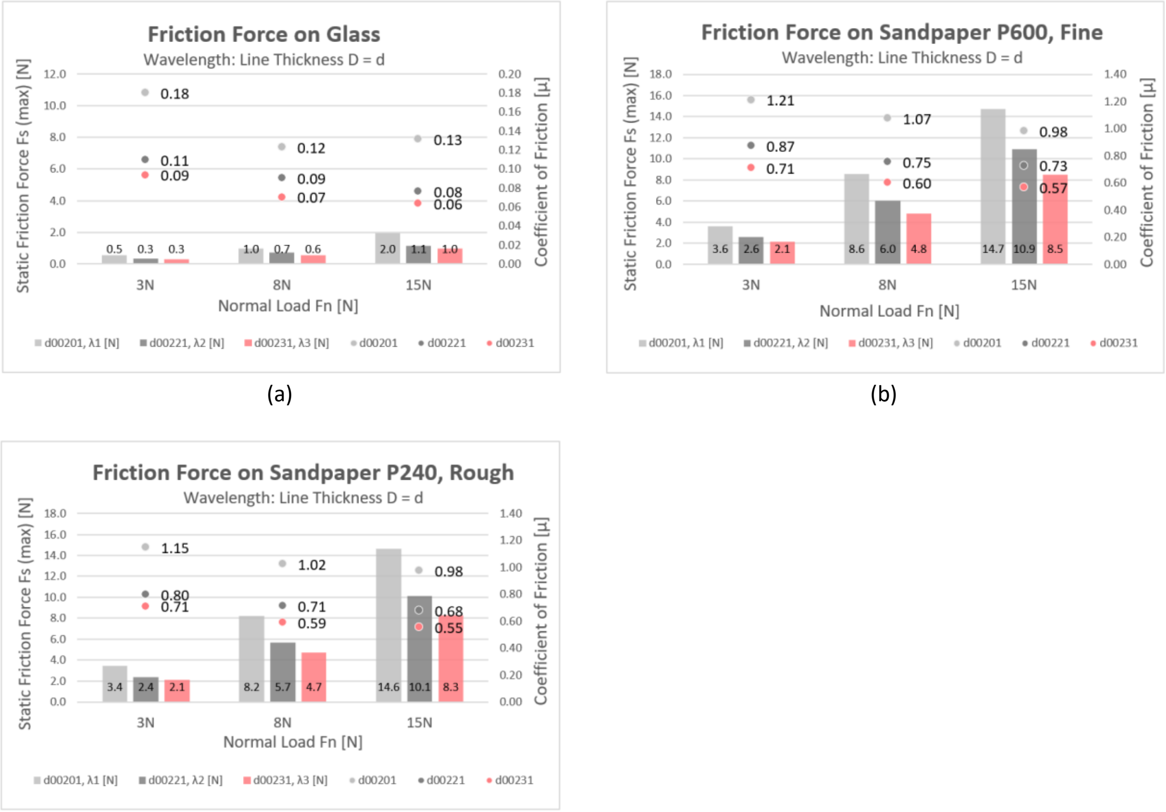

(a)

(b)

(c)

Figure 7.6. The maximum friction force (max.) F_s [N] and coefficient of static friction μ_s of 3D printed lines, with variable wavelength λ_1 = 2.8 mm, λ_2 = 1.8 mm and λ_3 = 0.8 mm with a correction value that disregards the effects of the number of printed features per mm^2 out, for the countersurface glass (smooth), sandpaper P600 (fine), and sandpaper P240 (rough). The measured F_s (max) is represented by columns and the corresponding μ_s is represented by dots.

The resulted μ_s are shown in Figure 7.6. It was observed that μ_s increased with increasing λ. This was the result of the increase in deformation with increasing λ, in which the 3D printed features had more room to deform. Comparing the results of Figure 7.5 and Figure 7.6, it can be concluded that a trade-off between both factors, i.e. the wavelength λ and the number density of the 3D printed features, should be taken into account

7.4. Local Features: Curvature (α)

The role of the angle α of curvature on the friction properties was analysed for the parameters α_1 = 0, α_2 = 68° with an inner radius of 16 mm and α_3 = 124° with an inner radius of 10 mm. The thickness d, height h and wavelength λ were kept constant, with a value of 0.5 mm, 4.0 mm and 1.8 mm, respectively, Figure 5.12. The F_s (max) and μ_s were measured for the 3D CAD models d00221, d00302, and d00303, Figure 7.8. For the curved patterns, i.e. model d00302 and d00303, the friction test was performed in both directions, Figure 7.7.

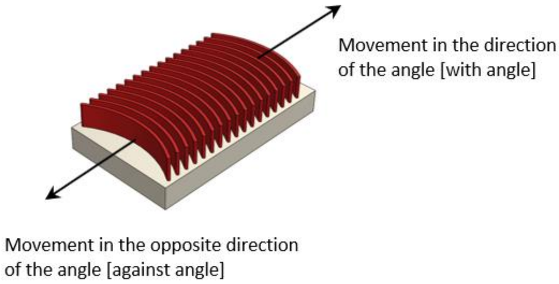

Figure 7.7. The direction of the movement during the friction test.

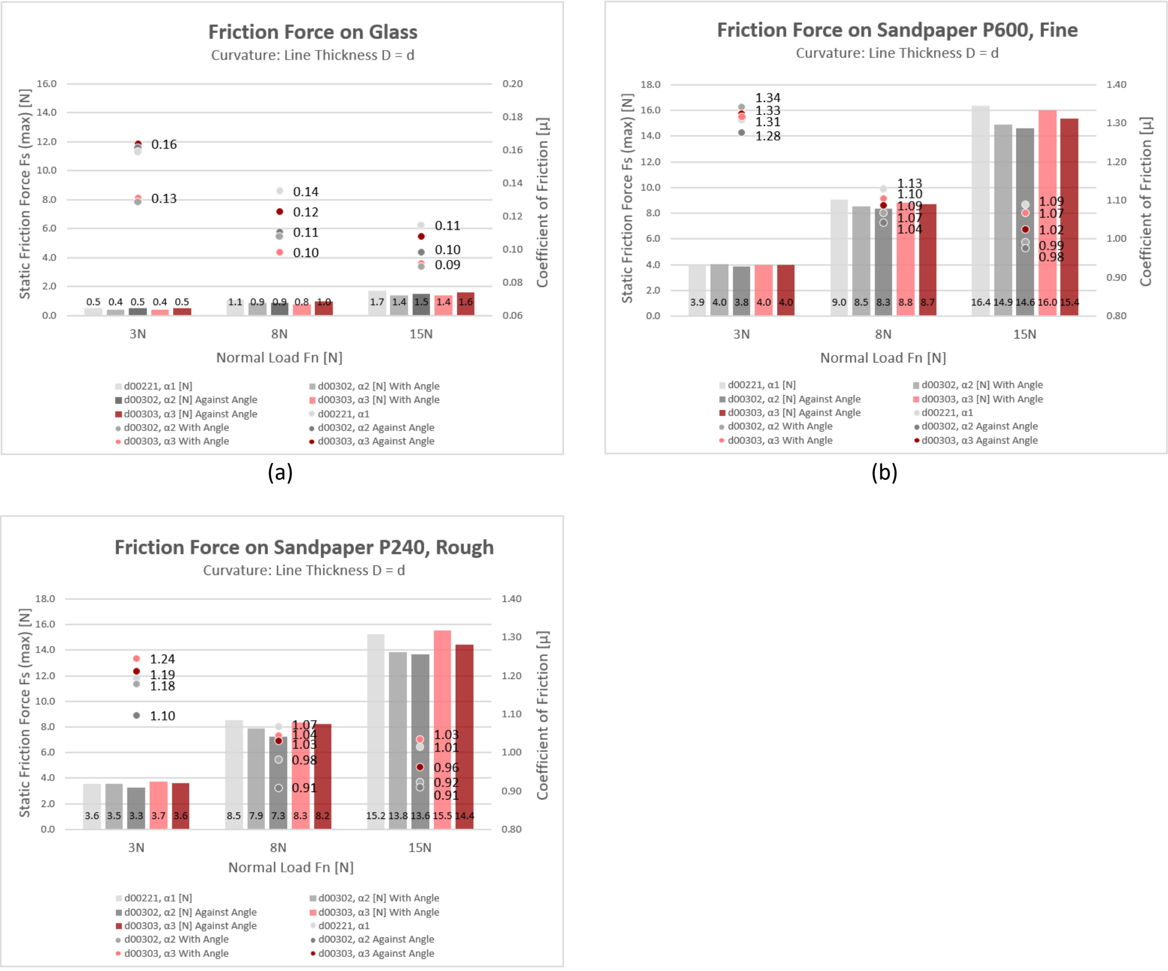

(a)

(b)

(c)

Figure 7.8. The maximum friction force (max.) F_s [N] and coefficient of static friction μ_s of 3D printed lines, with variable angle $\alpha_1 = 0°$, $\alpha_2 = 68°$ with an inner radius of 16 mm, and $\alpha_3 = 124°$ with an inner radius of 10 mm, for the countersurface glass (smooth), sandpaper P600 (fine), and sandpaper P240 (rough). The measured F_s (max) is represented by columns and the corresponding μ_s is represented by dots.

It was observed that the printed features displayed less deformation with increasing α. So, the straight lines of model d00221 (α_1) display more deformation compared to the almost circular curvature of model d00303 (α_3). Comparing the two curvatures, it was observed that a more circular curvature α_3 (compared to α_2), and moving the sample in the direction of the angle (referred to as 'with angle') displayed a slightly higher μ_s on a rough countersurface, Figure 7.8b-c. It is plausible that this phenomenon was the result of direction-dependent pattern deformation, in which the samples displayed more deformation when moving in the direction of the angle of the curvature.

7.5. Conclusion

The role of 3D printed surface features on the friction properties was analysed for pillar and/or line thickness *d*, tip thickness *D,* and wavelength λ. Despite small differences in μ_s of the small 3D printed area, some consistent trends were found:

- μ_s generally increases with increasing thickness *d*, i.e. for the distribution of the 3D printed features in straight patterns of pillars and lines (D = d);

- μ_s is influenced by the shape and curvature alignment of the 3D printed features. Take, for example, the T-shaped (D > d) 3D printed features. The surface friction of the T-shapes is determined by the deformation-term (influenced by thickness *d*) and the so-called adhesion-term, in which the contact area places an important role (influenced by the tip geometry *D*);

- μ_s increases with increasing wavelength λ, due to the increasing room for deformation of the 3D printed features. However, a positive correlation between the number density of the 3D printed features and the friction has been observed. Therefore, increasing the λ furthermore will result in a decreased number density of the 3D printed features, thus decreasing the adhesion-term of the overall friction.

- μ_s increases with increasing curvature α, up to a point in which a higher α increases the overall stiffness of 3D printed features.

- $\mu_s = \left(\mathrm{F}_{\mathrm{f,adh}} + \mathrm{F}_{\mathrm{f,def}}\right)/\mathrm{F}_{\mathrm{n}}$ decreases under increasing F_n. This phenomenon can be explained due to the flattening of the 3D printed features under increasing load, in which the deformation-term contributes less-and-less to the overall friction.

- μ_s is the lowest for the smooth, glass countersurface and the highest for the fine sandpaper P600. The most probable reason is that the asperities of the sandpaper countersurface resulted in an additional interlockings, thus increasing the overall μ_s. However, this is not the case for the smooth, glass surface in which the (micro)asperities are far smaller compared to the minimal printable thickness of the 3D printed features.

Based on the collected results, various patterns consisted of curvatures, wave-liked, or circular patterns with varying α were analysed further, Chapter 9.

8. CONCEPTUAL DESIGN: COMBINED VARIABLES

8.1. Retesting 3D FDM Print Conditions: Changing the Filament TPU 95A (Spool B)

The previous 3D printed samples were printed with the same TPU filament (spool A). During the experimental study, a new batch of TPU filament (spool B) was loaded in the printer. After the first test, it was immediately clear that the 3D printed features of spool B did not showed the same elastic properties under the same print conditions. The new 3D printed features were thicker and thus stiffer than before. The 3D CAD thickness of 0.5 mm for the 3D printed features, resulted in a real printed thickness of 0.35 – 0.4 mm for spool A and a real printed thickness of 0.55 – 0.6 mm for spool B, under similar print conditions. The minimal print thickness, which was initial set on 0.5 mm for spool A in Chapter 5.1, could now be set to 0.4 mm for spool B. However, the new real printed thickness of 0.45 – 0.55 mm still displayed more stiffness compared to the previous 3D printed lines. Changing the print speed and print temperature did not change this phenomenon.

8.2. Wave Pattern

The role of the thickness *d*, tip thickness *D*, wavelength *λ*, and curvature *α* of the 3D printed features on the surface friction properties was analysed. Based on the results in Chapter 7, the thickness *d*, height *h,* and wavelength λ were set on 0.4 mm, 4.0 mm and 1.8 mm, respectively. Different patterns were created next that combined the resulting optimum parameters on the friction properties. The following wave patterns, consisting of peaks in the opposite directions, were analysed for the parameters $\alpha_1 = 24°$ with an inner radius of 16 mm and $\alpha_2 = 49°$ with an inner radius of 8 mm. The 3D CAD models d00401, and d00501 consisted of a total of 18 and 14 lines, respectively, Figure 8.1.

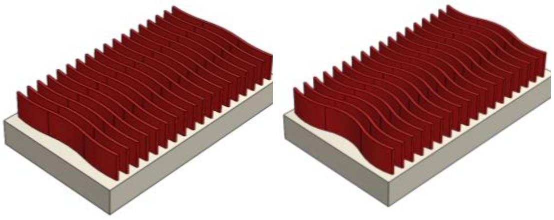

Model Nr.	**d00401**	**d00501**
d [mm]	0.4	0.4
h [mm]	4.0	4.0
λ [mm]	1.8	1.8
α [°]	α_1	α_2

Figure 8.1. The wave patterns with variable angle $\alpha_1 = 24°$ with an inner radius of 16 mm and $\alpha_2 = 49°$ with an inner radius of 8 mm.

The 3D printed wave patterns are shown in Figure 8.2.

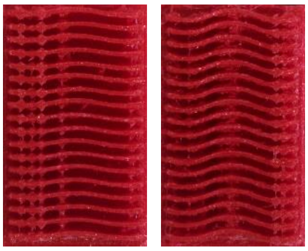

Model Nr.	d00401	d00501
α [°]	α_1	α_2

Figure 8.2. Top view of the 3D printed wave patterns with variable angle $\alpha_1 = 24°$ with an inner radius of 16 mm and $\alpha_2 = 49°$ with an inner radius of 8 mm.

8.3. Circular Pattern

Like the previous wave pattern, the following circular patterns consisted of curves α in the opposite directions. The curves α of 3D CAD model d00601 were similar to model d00302, with an angle of 68° and inner radius of 16 mm. However, these curves were halfway placed in the opposite direction and thus simulated a circular pattern. The model d00601 consisted of a total of 10 curves. The 3D CAD model d00701 consisted of a circular shape as a starting point with an inner diameter of 3.5 mm and consisted of a total of four circular lines and four curvatures at the end. The 3D CAD model d00801 was similar to d00701; however, instead of circular shape as a starting point, the model simulated a combined shape of a square and half a circle on each end. Both the square and circle of both consisted of an inner diameter of 3.5 mm, Figure 8.3. The thickness *d*, height *h,* and wavelength λ were kept constant for all three models, with a value of 0.4 mm, 4.0 mm and 1.8 mm, respectively.

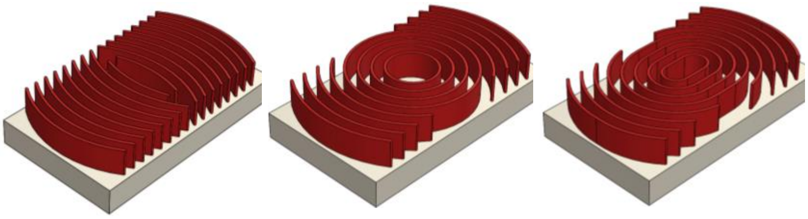

Model Nr.	d00601	d00701	d00801
d [mm]	0.4	0.4	0.4
h [mm]	4.0	4.0	4.0
λ [mm]	1.8	1.8	1.8

Figure 8.3. The circular pattern models consist of (a) 68° curvatures and an inner radius of 16 mm (d00601), (b) a circular shape as the starting point with an inner diameter of 3.5. mm (d00701), (c) and a combined shape of a square and half a circle with each an inner diameter of 3.5 mm (d00801).

The 3D printed circular patterns are shown in Figure 8.4. During initial printing of the circular pattern d00701 and d00801, it was immediately clear that the circular shape in the middle with a small(er) diameter as starting point, resulted in a very stiff (almost rigid) circle with a lot of additional material in the middle. After further testing, the diameter was set on 3.5 mm.

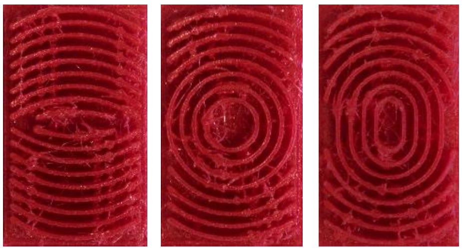

Model Nr.	d00601	d00701	d00801
α [°]	α_1	x	x

Figure 8.4. Top view of the 3D printed circular pattern with (a) 68° curvatures and an inner radius of 16 mm (d00601), (b) a circular shape as the starting point with an inner diameter of 3.5. mm (d00701), (c) a combined shape of a square and half a circle with each an inner diameter of 3.5 mm (d00801).

8.4. Final Pattern Design

The effects of the previous patterns on the surface friction properties were analysed. Based on these results, a final pattern was created combing curves with a wave-like pattern in a circular-shaped pattern. The 3D CAD models d00901 and d00911 consisted of a total of ten curvatures of $\alpha_1 = 68°$ with an inner radius 16 mm, eight waves of $\alpha_2 = 49°$ with an inner radius of 8.0 mm, and a thickness $d_1 = 0.4$ mm for model d00901 and $d_2 = 0.8$ mm for model d00911. The height *h* and wavelength λ were kept constant, with a value of 4.0 mm and 1.8 mm, respectively, Figure 8.5. Detailed drawings of the 3D printed pattern d00901 can be found in Appendix C.

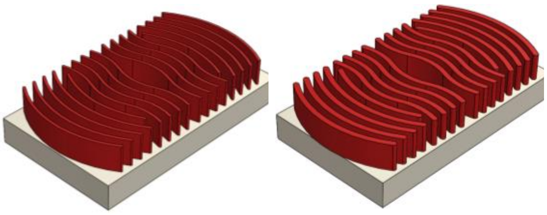

Model Nr.	d00901	d00911
d [mm]	d_1	d_2
h [mm]	4.0	4.0
λ [mm]	1.8	1.8
α [°]	α_1, α_2	α_1, α_2

Figure 8.5. The final patterns with a total of 10 curvatures with an inner radius 16 mm (68°), 8 waves with an inner radius of 8.0 mm (49°), and a variable thickness $d_1 = 0.4$ mm (d00901) and $d_2 = 0.8$ mm (d00911).

The final 3D printed patterns are shown in Figure 8.6.

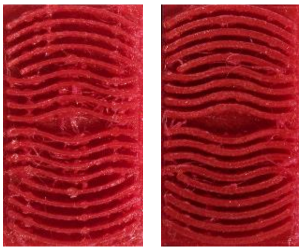

Model Nr.	**d00601**	**d00701**
d [mm]	d_1	d_2

Figure 8.6. Top view of the final 3D printed pattern with a total of 10 curvatures with an inner radius 16 mm (68°), 8 waves with an inner radius of 8.0 mm (49°), and a variable thickness d_1 = 0.4 mm (d00901) and d_2 = 0.8 mm (d00911).

9. EXPERIMENTAL RESULTS: COMBINED VARIABLES

9.1. Retesting of the Printed Samples: Changing the filament TPU 95A (Spool B)

As mentioned in Paragraph 8.1, a new batch of TPU filament was used in the next step. The sample of spool B displayed less deformation compared to spool A. The 3D CAD model d00302 was reprinted with spool B to compared with spool A during the experiment. The F_s (max) and μ_s wear were measured for model d00302 printed with spool A and spool B, Figure 9.1.

(a)

(b)

(c)

Figure 9.1. The maximum friction force (max.) F_s [N] and coefficient of static friction μ_s of 3D printed lines, with variable angle α_1 = 0°, α_2 = 68° with an inner radius of 16 mm, and α_3 = 124° with an inner radius of 10 mm, for the countersurface glass (smooth), sandpaper P600 (fine), and sandpaper P240 (rough). The measured F_s (max) is represented by columns and the corresponding μ_s is represented by dots.

An increase in μ_s was observed for spool B for the countersurface sandpaper. On the other hand, a decrease in μ_s was observed for spool B for the countersurface glass. This might be the result of less elastic properties of the new printed features, which resulted in less contact area between the two surfaces.

9.2. Wave Pattern

As mentioned before, a curved pattern resulted in a direction-dependent pattern deformation in which the direction of the peak and valley was observed to influence F_s. Therefore, a more wave-like pattern, with peaks in opposite direction, was analysed next. The previous half circular curvature of model d00303 (Paragraph 5.6) displayed a much stiffer structure, due to the print conditions; the angle and direction of the print head resulted in slightly thicker and thus stiffer corners. In order to minimize the effect of the print process, a wave-like pattern was created for the parameters $\alpha_1 = 24°$ with an inner radius of 16 mm and $\alpha_2 = 49°$ with an inner radius of 8 mm. The F_s (max) and μ_s were measured for the 3D CAD models d00401, and d00501. The results of the model d00401 and d00501 were compared to their counterpart d00221 of straight lines, Figure 9.2.

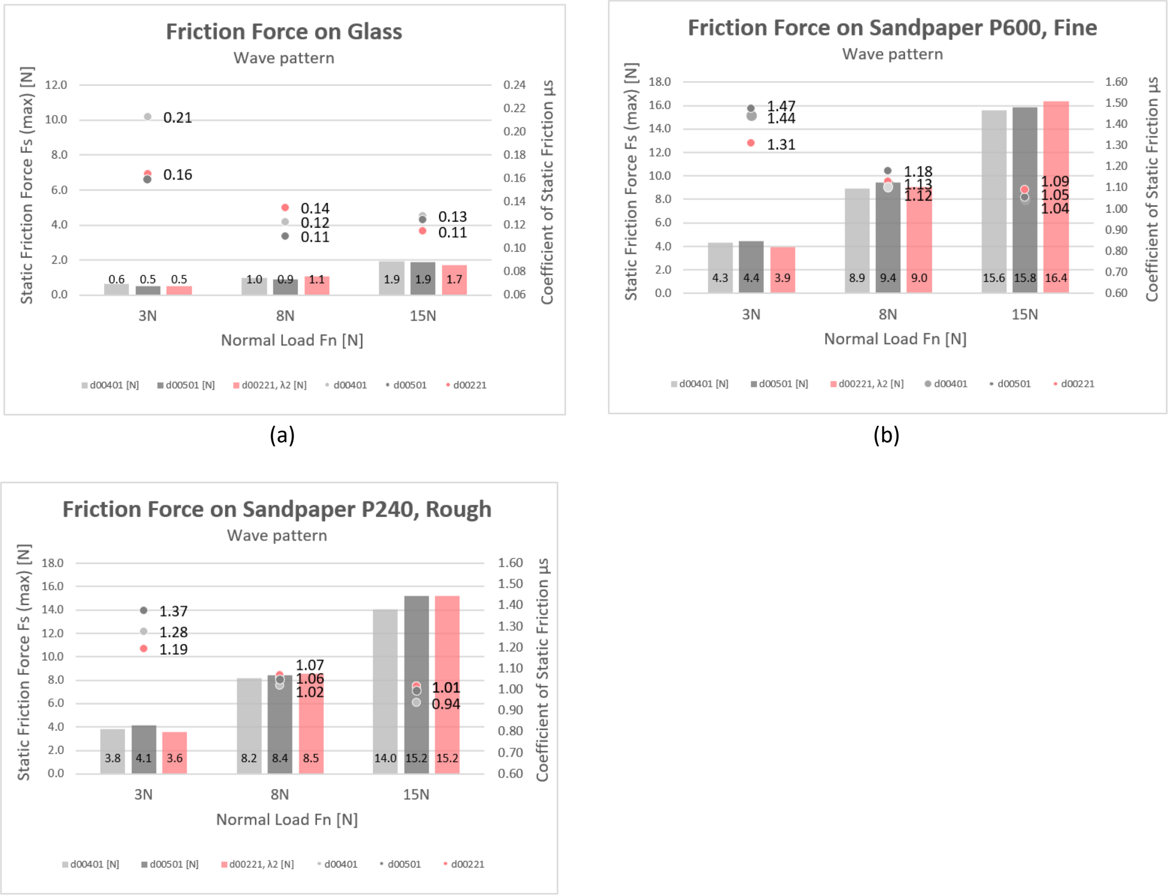

(a)

(b)

(c)

Figure 9.2. The maximum friction force (max.) F_s [N] and coefficient of static friction μ_s of 3D printed straight lines (d00221) and wave patterns, with variable angle $\alpha_1 = 24°$ with an inner radius of 16 mm (d00401) and $\alpha_2 = 49°$ with an inner radius of 8 mm (d00501), for the countersurface glass (smooth), sandpaper P600 (fine), and sandpaper P240 (rough). The measured F_s (max) is represented by columns and the corresponding μ_s is represented by dots.

Similar to Paragraph 7.4, an slight increase in μ_s was observed for an increasing angle.

9.3. Circular Pattern

In the previous paragraph, the role of the angle of the curvature of a wave-like pattern was analysed. In the next step, the angle of a more circular pattern was analysed. The thickness *d*, height *h,* and wavelength λ were kept constant for all three models, with a value of 0.4 mm, 4.0 mm and 1.8 mm, respectively. The F_s (max) and μ_s were measured for the 3D CAD models d00601, d00701, and d00801, Figure 9.3.

(a)

(b)

(c)

Figure 9.3. The maximum friction force (max.) F_s [N] and coefficient of static friction μ_s of 3D printed circular patterns with: (a) 68° curvatures and an inner radius of 16 mm (d00601), (b) circular shape as the starting point with an inner diameter of 3.5. mm (d00701), (c) and a combined shape of a square and half a circle with each an inner diameter of 3.5 mm (d00801) , for the countersurface glass (smooth), sandpaper P600 (fine), and sandpaper P240 (rough). The measured F_s (max) is represented by columns and the corresponding μ_s is represented by dots.

It was observed that the circular patterns (d00701 and d00801) resulted in a slightly higher μ_s on a smooth, glass countersurface, while for sandpaper this was the case for pattern d00601. The latter is highly likely to be the result of better interlocking mechanism between pattern d00601 and the sandpaper countersurface.

9.4. Final Pattern Design

Based on the previous results, the final pattern design combined curves and waves of varying angle in a circular pattern. The height *h* and wavelength λ were kept constant, with a value of 4.0 mm and 1.8 mm, respectively, Figure 8.5. Note that so far, the thickness *d* was set on the smallest thickness of 0.4 mm to more clearly analyse the role of direction-dependent pattern deformation on the friction properties. Therefore, the F_s (max) and μ_s were measured for the 3D CAD models d00901 (d_1) and d00911 (d_2), with a thickness of 0.4 mm and 0.8 mm, respectively. The results of the patterns d00401 – d00911 are all shown in Figure 9.3.

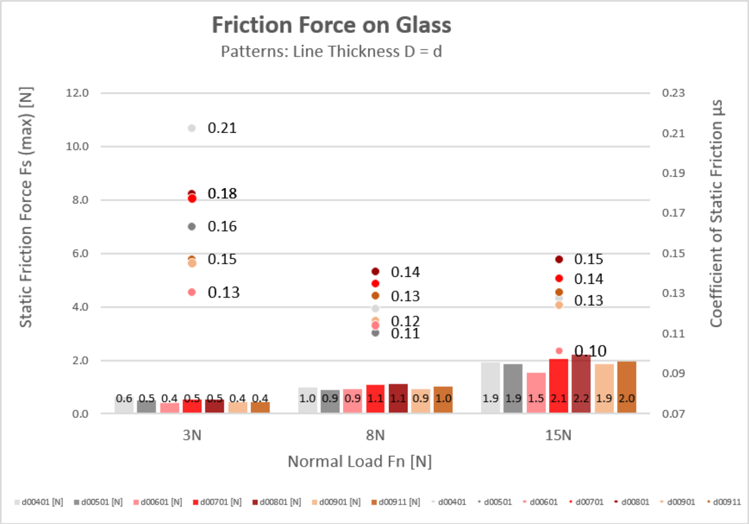

(a)

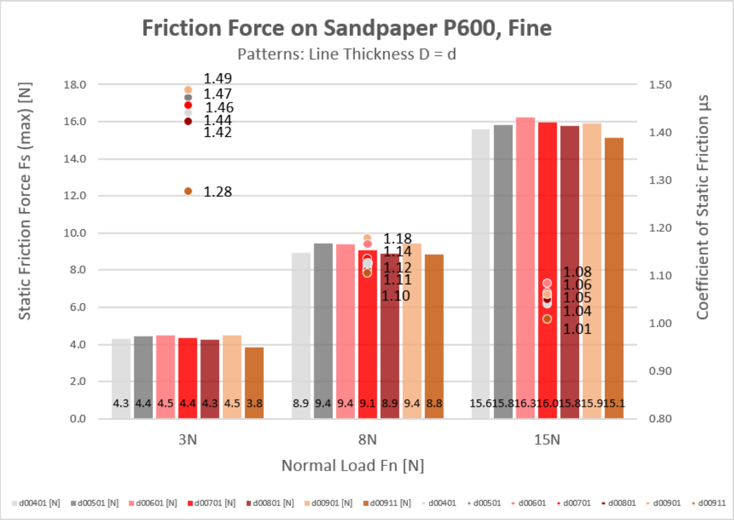

(b)

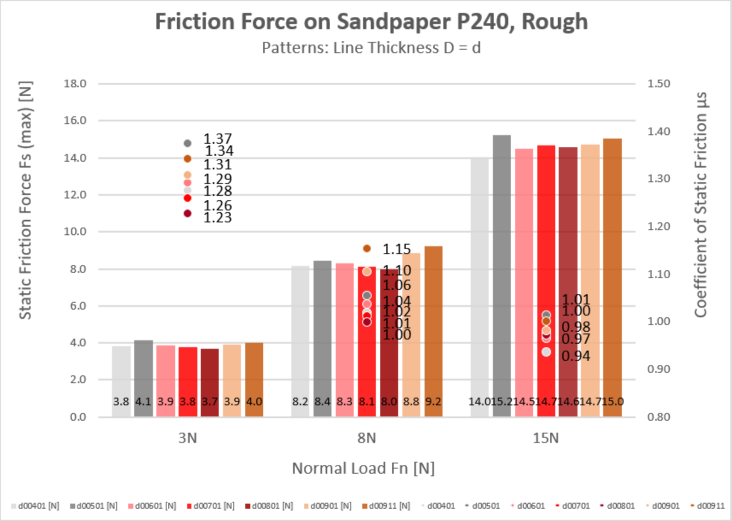

(c)

Figure 9.4. The maximum friction force (max.) F_s [N] and coefficient of static friction μ_s of 3D printed patterns: d00401 (d_1) light grey, d00501 dark grey (d_1), d00601 (d_1) pink, d00701 (d_1) light red, d00801 (d_1) dark red, d00901 (d_1) light orange, and d00911 (d_2) dark orange, with thickness d_1 = 0.4 mm and d_2 = 0.8 mm, for the countersurface glass (smooth), sandpaper P600 (fine), and sandpaper P240 (rough). The measured F_s (max) is represented by columns and the corresponding μ_s is represented by dots.

As shown in Figure 9.4, there was no clear winner for al testing scenario, i.e. the varying normal forces and countersurfaces. For the smooth, glass countersurface a slightly higher μ_s was observed for the circular patterns d00701 and d00801 compared to pattern d00901. An increase in the μ_s was observed for the higher thickness of model d00911 (d_2) compared to model d00901 (d_1) for the countersurface glass and sandpaper P240. It is plausible that in those cases, the $\mathrm{A_{real}}$ was the dominating factor, Figure 9.4a. and Figure 9.4c. However, this was not the case for the finer sandpaper P600, in which an interlocking mechanism due to the smaller thickness d_1 was the dominating factor, Figure 9.4b.

10. FUNCTIONAL TESTING

10.1. 3D Printed Fingertips

The goal of this experimental study is to engineer a bio-inspired surface structure to improve the grip action of prosthetic hands and to evaluate the low-cost 3D printing technology for this purpose. The 3D printed patterns were initially printed on a flat, rigid surface. However, the patterns were designed with the idea of future integration with 3D printed prosthetic hands. A detailed description of the 3D printed prosthetic hand considered in this study can be found in Cuellar et al. [4], Figure 10.1.

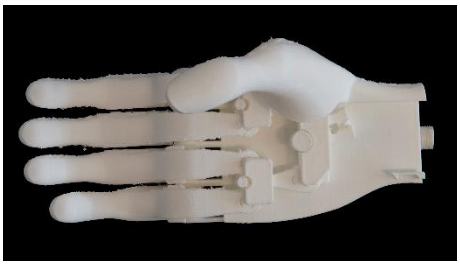

Figure 10.1. The 3D printed prosthetic hand used in the functional testing [4].

To test the effect of the patterns on surface friction, a more practical settings is needed. Therefore, the patterns of the CAD model d00901 (d_1 = 0.4 mm) and d00911 (d_2 = 0.8 mm), described in Chapter 8.4, were tested directly on a prosthetic hand. The patterns were printed onto a hollow, glove-liked fingertip structure that could slid onto the 3D printed prosthetic hand. The original fingertip design of the prosthetic hand consisted of the rigid PLA material. The grip action of the original design was compared with three different 3D printed fingertips made from elastic TPU: a flat fingertip; a fingertip with the pattern d00901 (referred to next as pattern-d_1); and a fingertip with the pattern d00911 (referred to next as pattern-d_2), Figure 10.2. A total amount of 4 similar index fingertips, and one thumb per design were printed. A detailed description of the index fingertip can be found in Appendix D.

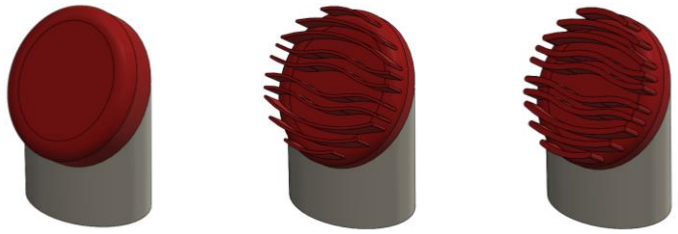

Model Nr.	**Index Fingertip Flat**	**Index Fingertip Model d00901**	**Index Fingertip Model d00911**
d [mm]	x	d_1	d_2
h [mm]	4.0	4.0	4.0
λ [mm]	x	1.8	1.8

Figure 10.2. The 3D printed index fingertips for the functional testing, with (a) a flat surface or (b-c) a pattern on top.

In the previous experiments, these patterns were printed on a flat rectangular shape, Chapter 5. However, to mimic the shape of a human fingertip, the patterns were printed on to a flat, oval and, slightly less rigid surface. The latter was the result of the rounded edges of the 3D CAD model, which likely reduced the stress concentration in the 3D printed object. Therefore, it is highly likely that the rounded edges decrease the rigidity of the underlying surface structure on which the patterns are printed.

The hollow cylindrical shape and pattern on top, made for a challenging 3D printing process. Both the support of the hollow shape and pattern were taken into consideration. The attempts to print the hollow cylindrical shape in either a horizontal position, a vertical position, or a position close to 45° failed due to inadequate supporting. In addition, due to the layer-by-layer fashion of the 3D print technology, the 3D printed features perpendicular to the printing plane displayed a decrease in dimensional accuracy due to the so-called ‘staircase effect’. The staircase effect in 3D printing is a phenomenon in which the layer marks are clearly visible at the surface. The decrease in accuracy resulted in holes or gaps in the 3D printed lines of the pattern. The fingertips were printed in a slightly angled position, to mimic the angle in which the pattern would have been printed on the original 3D prosthetic hand. An additional support structure was added. However, due to the fact that the surface area on which the patterns were printed was not horizontal, compared to the test sample in Chapter 7 and 9, a reduction in the print accuracy of the small features was observed, especially for thickness d_1.

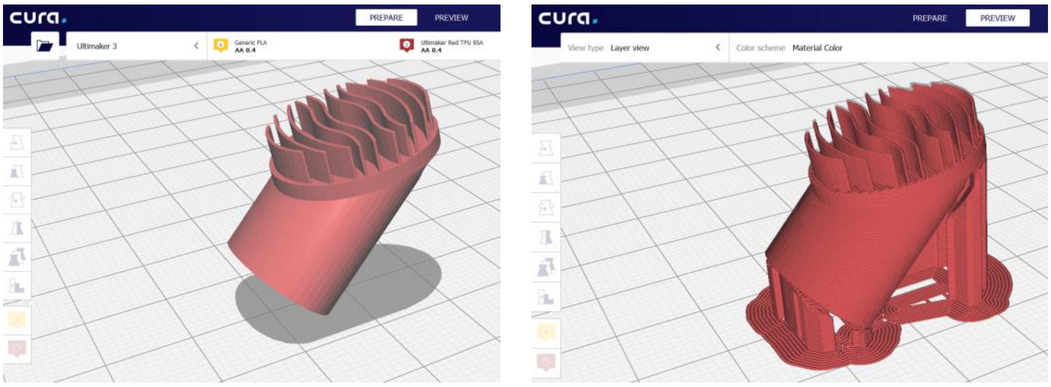

Figure 10.3. The positioning of the 3D CAD fingertip in the slicing software Cura.

10.2. Box and Blocks Test (BBT)

The hollow 3D printed fingertips were slid onto the 3D printed prosthetic hand. The 3D printed body power prosthetic hand in question was attached to a cuff that was strapped around the user’s dominant forearm. The prosthetic hand is driven by a pulling cable attached to the opposite shoulder and connected to the mechanism that connects the four index fingers. Extending the arm results in the pulling of the cable, and consequently, opening and closing the fingers of the prosthetic hand [45]. The fingertips were assessed using the Box and Blocks Test (BBT) [46], to evaluate the prosthetic design with the users. The BBT test is composed of a box divided into two separated areas by a partition in the middle, and 25-mm wooden square cubes. The prosthetic users were asked to move as many blocks as possible, one-by-one, from one container to the other, within 60 seconds, Figure 10.4.

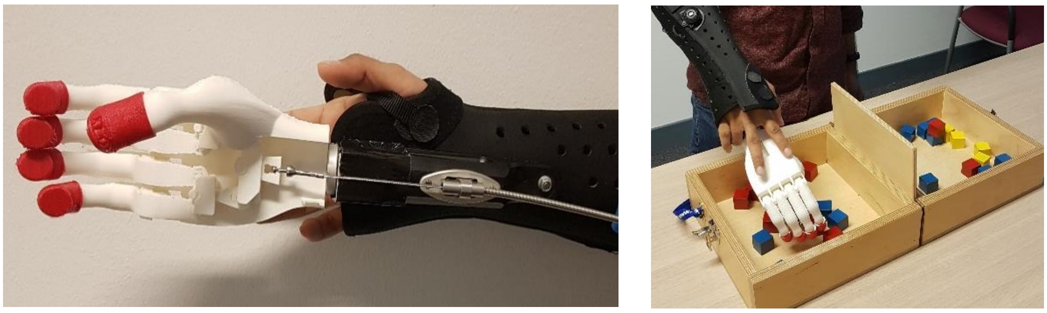

(a) (b)

Figure 10.4. (a) the 3D printed fingertips attached to the 3D printed prosthetic hand; (b) the Box and Blocks Test setup.

10.3. Results

A total of 3 right-handed students of the of the Delft University of Technology (2 males and 1 female; age: 22–27 years) were recruited. For each design the experiment was tested three times. The users were allowed a trail period prior to the testing, to get familiar with the body powered hand prothesis. The number of blocks moved from one container to another was used as reference value of the test performed with the different 3D printed fingertips. The BBT score are shown in Figure 10.5. The median score of the last trial (round 3) were 24, 33, 32 and 41 blocks for the original, the flat, the pattern-d_2 and the pattern-d_1 fingertip, respectively. The original fingertip-design scored the lowest (21-26 blocks moved within 60 seconds), while the pattern-d_1 scored the highest (36-43 blocks moved within 60 seconds). The flat fingertips and the stiffer fingertip pattern-d_2 showed similar results. The fingertip pattern d_1 resulted in a ~70% increase in the number of blocks moved compared to the original rigid PLA fingertip.

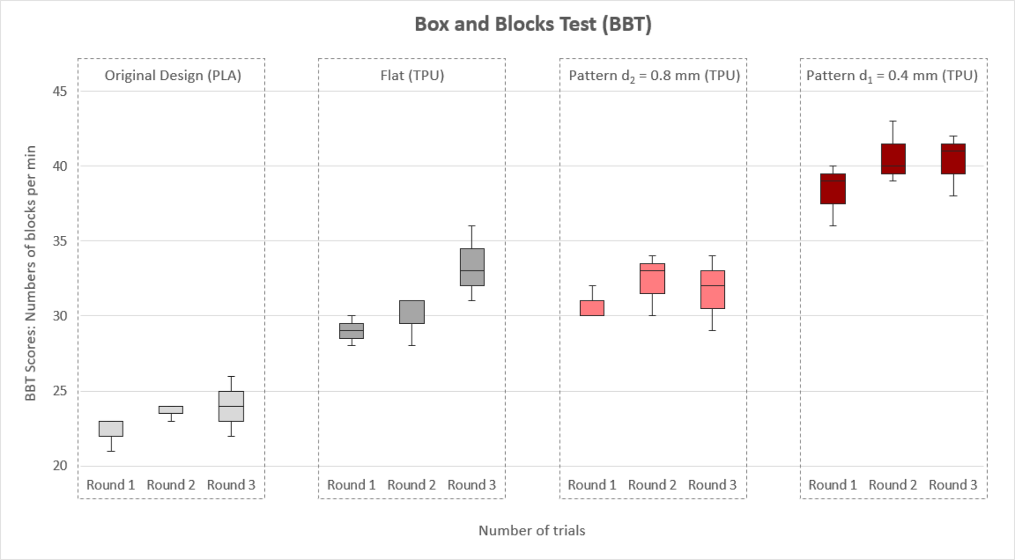

Figure 10.5. BBT scores for the 3D printed fingertips, redirected from left to right: the original fingertip design (PLA), the flat fingertip (TPU), the pattern $d_2 = 0.8$ mm (TPU), and the pattern $d_1 = 0.4$ (TPU).

The wooden squared blocks consisted of a relatively smooth surface. The previous results, discussed in paragraph 9.4, have indicated that an increase in μ_s is observed with increasing pattern thickness *d* on a smooth surface. The hypothesis was therefore that the pattern-d_2 would perform better compared pattern-d_1. However, real-life grasping scenarios are not only based on two flat surfaces moving parallel to each other, such as the experimental study in Chapter 6. The 3D printed surface features of pattern-d_1 displayed more deformation compared to pattern-d_2. Therefore, pattern-d_1 was able to grasp the squared blocks in more different ways compared to the flat fingertips and the stiffer pattern-d_2. The corners of the squared blocks could be held stable between the 3D printed features of the patterns, Figure 10.6c. Also, the original, rigid PLA fingertip design resulted in less contact area between the fingertips and the squared blocks (Figure 10.6a), compared to the soft, TPU flat fingertip (Figure 10.6b). The original fingertip resulted in more slipping of the blocks from the prosthetic hand during testing. It can be concluded that the shape itself (and thus the contact area) of the TPU flat fingertip increases the grip compared to the original design. However, if we compare the flat TPU fingertip with that of the pattern-d_1 an additional ~25% increase in the number of blocks moved, can be observed for the pattern-d_1.

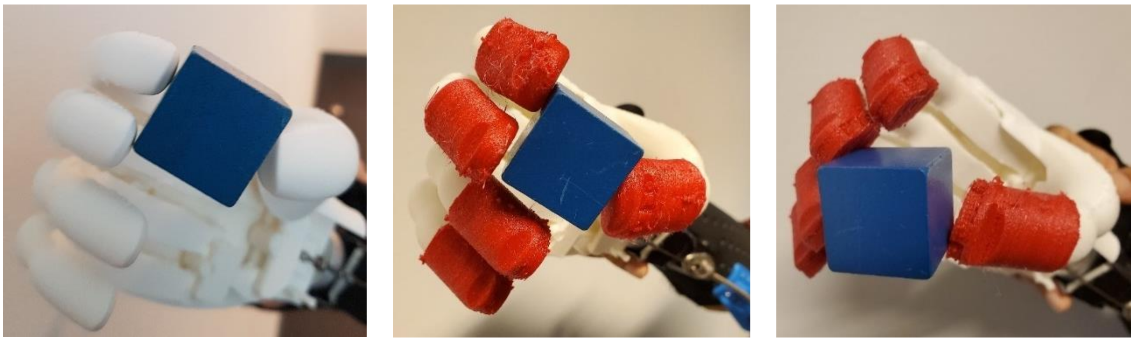
(a) (b) (c)

Figure 10.6. The graphing of a block between the (a) the original fingertips, (b) the flat fingertips, and (c) the pattern-d_1 fingertips.

10.4. User Performance

The BBT with the different fingertips was performed in the following order: the original fingertip design, the flat fingertip, the pattern-d_2, and the pattern-d_1. As shown in Figure 10.5, the BBT scores increased with the order of the test. Therefore, an additional trial (round 4) was performed after completing the BBT for all fingertips, to analyse the user's learning curve for the increased BBT scores. The results are shown in Figure 10.7. The median score of the additional trial (round 4) were 27, 34, 33 and 43 blocks for the original, the flat, the pattern-d_2 and the pattern-d_1 fingertips, respectively. Again, the original fingertip design scored the lowest, while the pattern-d_2 fingertips scored the highest (~60% increase). Therefore, it can be concluded that the user's learning curve did not significantly influence the test results.

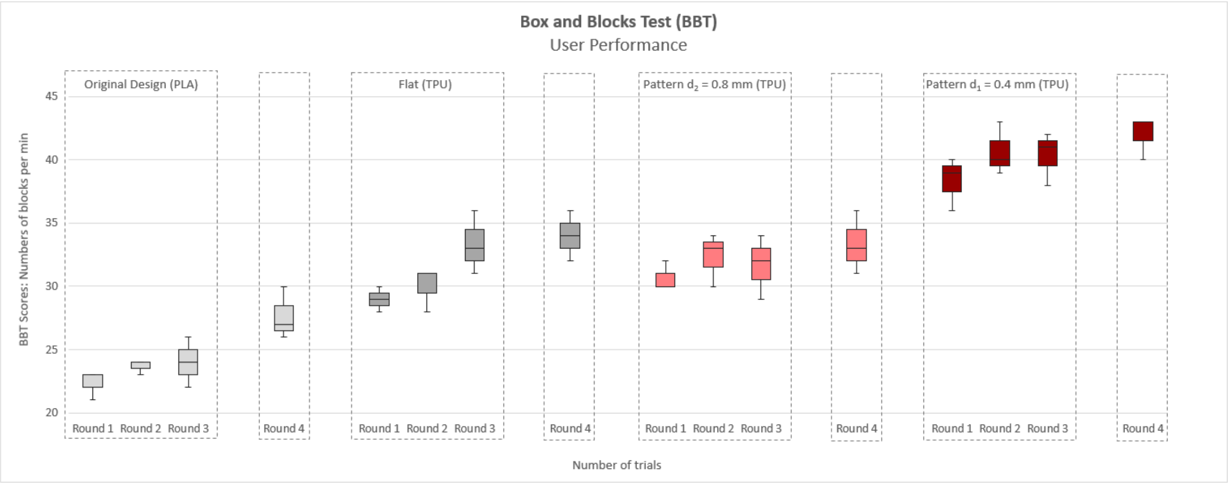

Figure 10.7. BBT scores for the 3D printed fingertips, redirected from left to right: the original fingertip design (PLA), the flat fingertip (TPU), the pattern $d_2 = 0.8$ mm (TPU), and the pattern $d_1 = 0.4$ (TPU) with the additional round 4.

A survey was conducted at the end of the BBT test. The NASA Task Load Index (TLX) method was used to analyse the physical demand, performance, and effort of the users during each test. A number rating scale was used from 1 to 10, in which 1 = Very Low and 10 = Very High. The survey indicated only a slightly higher Load Index for the original fingertip (i.e., an average TLX value of 5.6), compared to the TPU fingertips (i.e., an average TLX value of 4.3), due to the higher risk in slipping of the blocks from the original prosthetic hand during testing

10.5. Dirt Test

A rough contact surface usually ensures dirt to stick easily to the surface. This is even more the case for the relatively large (i.e., the height *h*) 3D printed surface features. The fingertip pattern-d_2 was dipped in a bucket of slightly moist soil, to test the effect of dirt between the pattern on the grip action. After each fingertip was dipped in soil, the BBT test was performed again with one user. The results are shown in Figure 10.8. The results indicated that dirt between the 3D printed features did not influence the grip action.

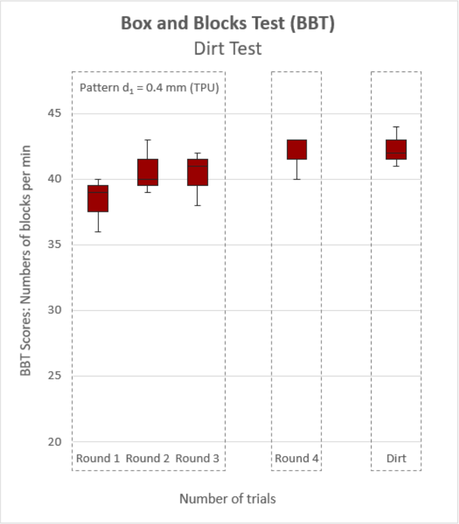

Figure 10.8. BBT scores for the 3D printed fingertip pattern d_1 = 0.4 (TPU), for clean fingertips (round 1-4), and for fingertips dipped in soil (round 'dirt').

The soil between the fingertip pattern fell off bit by bit during testing, which resulted in almost clean fingertips after finalizing the BBT. Figure 10.9 shows the soil between the fingertip patterns before the BBT (left) and after the test (right). Afterwards, the additional soil was then easily washed away.

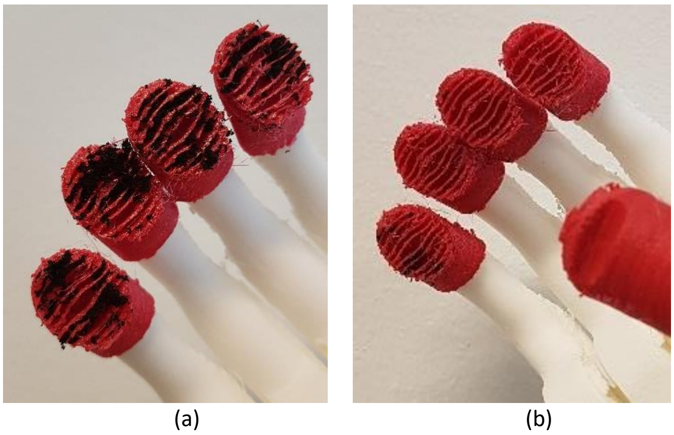
(a) (b)

Figure 10.9. The 3D printed fingertip pattern d_1 = 0.4 (TPU) with soil between the fingertips: (a) before and, (b) after the BBT.

11. DISCUSSION

11.1. Introduction

Commercial prosthetic hands are still limited in their grasping ability, such as the adaptability to the shape of an object and a sufficient pinch force level for practical use. The goal of this experimental study is to analyse the frictional characteristic of (deformable) surface patterns and to evaluate the FDM 3D printing technology for this purpose. The 3D printed features were designed with the idea of future integration with 3D printed prosthetic hands, such as presented by Cuellar et al. [4], to improve their grip action. 3D printed prosthetic hands, generally consist of rigid materials. On the contrary, human fingertips and various biological adhesive surface consist of deformable surface structures, which allows for adaptability and uniform distribution of stress.

11.2. 3D Printing of the Flexible TPU 95A

To analyse the contact mechanism of deformable 3D printed surface features, the flexible and abrasion-resistant Thermoplastic Polyurethane (TPU) 95A Red was used. The 3D printed (deformable) features were printed on top of a rigid surface. The 3D printed features consisted of pillars or lines varied in thickness *d*, tip thickness *D,* wavelength *λ,* and curvature α. The flexible thermoplastic showed various challenges when it came to small dimension printing with the FDM 3D printer; Ultimaker 3.

First, a large discrepancy in printing accuracy was observed between the 3D printed features. The large print discrepancy was especially the case for 3D printed pillars with a diameter of less than 0.8 mm, and a height less than 2 mm. The direction of the print head was observed to highly influences the shape of the pillars, and thus the print accuracy. Lowering the print speed and printing temperature might minimize the effect of the print head' direction on the pillar shapes, but it will drastically lower the production time. In addition, the low pillar height resulted in features that were not clearly distinguished from another and did not display any deformation. To clearly observed the roll of the deformable patterns on the grip action, the benchmark for the pillar height *h* was set to 4 mm. The optimal pillar height for an optimal grip has not been studied further. Also, the low print accuracy initially resulted in the fusion of the 3D printed features. A minimal wavelength of 1.2 mm was used to avoid the fusion of the 3D printed features, especially with pillars. 3D printed lines were preferred to pillars, due to better printing accuracy and wear resistant.

Next, the minimum print diameter of 0.4 mm occasionally resulted in holes or gaps in the layers. To minimize the gaps between the layers, a trade-off had to be made between the print thickness (and thus the deformation capacity of the 3D printed features), the print speed, the print direction and even the angle in which the 3D printed object is placed on the build plate. Due to the layer-by-layer fashion of the 3D print technology, the printed features displayed a decrease in print accuracy when printed at an angle (i.e., instead of vertical) due to the so-called 'staircase effect'. The staircase effect in 3D printing is a phenomenon in which the layer marks are clearly visible at the surface. The low print accuracy resulted in gaps in the 3D printed features, especially for the minimal print thickness of 0.4 mm.

Moreover, the flexible TPU was sensitive to the print speed, which occasionally resulted in the compression of the material, jamming of the material in the 3D printer's print head, and strings of material between parts of the original design. The latter was increasingly observed for the 3D printed curvatures compared to straights lines. Changing the placement at the build plate and print temperature of the printer did not change this phenomenon. However, increasing the wavelength and lowering the print speed minimized the additional material between the 3D printed features. After initial testing, the optimal print speed for the small features was set on 15 mm/s, instead of the default print speed of 25 mm/s. Considering that the 3D printed features experimented in this work will be used for 3D printed low-budget prosthetic hands, a trade-off needs to be made between the production time and the actual improvement in print accuracy.

Moreover, different filaments of TPU 95A displayed differences in material properties. TPU 95A Red of spool A was not able to print the minimal print thickness of 0.4 mm without significant gaps in the layers. The 3D CAD thickness was therefore set on 0.5 mm, which resulted in a real printed thickness between

0.35 – 0.4 mm. However, spool B resulted in a real printed thickness between 0.55 – 0.6 mm, under similar print conditions. The 3D CAD thickness for Spool B could then be lowered to a minimum thickness of 0.4 mm. Still, spool B resulted in a real printed thickness between 0.45 – 0.55 mm, which was larger compared to the minimal thickness achieved with spool A. In addition, the TPU 95 A filament of different colours (e.g., red and blue) seemed to display different elastic properties. TPU 95 A Red was observed to be softer (i.e., more elastic) compared to TPU 95 A Blue.

The low-cost Ultimaker 3, combined with the low-cost flexible TPU, showed relatively low print accuracy, especially for small dimension printing. The print settings adjusted for this purpose were: a layer height of 0.15 mm, an infill density of 10%, a print speed between 15 – 25 mm/s and a print temperature between 220 – 230°C. The print speed was observed to highly impact the 3D printed features while changing the temperature had no noticeable effect. Adapting the design and print settings for optimal printing of the 3D printed features presented in this study is a starting point. When it comes to highly accurate small dimensional features, traditional manufacturing techniques are still preferred over AM. However, AM technologies have rapidly improved in the last decade and, for instance, 3D lithography technology is able to print in nanoscale [47]. In addition, for the low-budget FDM 3D printer, smaller nozzles (such as the 0.25 mm nozzle of the Ultimate S3) and a variety of new flexible 3D printed materials are already available [48].

11.3. Friction Characteristic of deformable 3D Printed Surface Patterns

The friction characteristic of the (deformable) 3D printed surface features was analysed by systematically modifying different topographical parameters. The 3D printed patterns consisted of 3D printed pillars or lines varied in thickness *d*, tip thickness *D*, wavelength *λ,* and curvatures α, combined into different patterns. The 3D printed surface patterns were tested against three different countersurfaces: glass (smooth), sandpaper P240 (rough), and sandpaper P600 (fine). Despite small differences in the static coefficient of friction μ_s of the 3D printed patterns, some consistent trends were found.

First, μ_s generally increased with increasing thickness *d* for both pillars and lines (D = d). However, different shapes and curvature alignment resulted in direction-dependent pattern deformation of the 3D printed features, in which an increasing thickness *d* did not necessarily result in higher surface friction. Take, for example, the T-shaped (D > d) 3D printed features. The surface friction of the T-shape is determined by the deformation-term (influenced by thickness *d*) and the so-called adhesion-term (influenced by the tip geometry *D*). The 3D printed features' bending ability, combined with a direction-dependent pattern deformation, resulted in a contact mechanism in which the deformation-term is the dominating factor. Therefore, a lower thickness *d* can sometimes be preferred, depending on the pattern. Biological surfaces display gradients of mechanical properties and contact units, which are assumed the perfect example for optimized surface friction. In a way, the T-shaped 3D printed features display a gradient of mechanical properties. Further tests of different shapes and structures, different material (properties), multi-filament printing, and print conditions, are needed to more accurately create a bio-inspired surface which display gradients of mechanical properties for optimized surface friction. However, it should be considered whether current (FDM) 3D printing technology is realistically suitable for this task. There are few significant limitations to 3D printing compared to the biology, such as the limited available print material and the minimal print thickness. The limited print material consists of material properties that are different compared to the human skin. In addition, the minimal FDM 3D print thickness is limited to the nozzle thickness and material properties. In this experimental study, a minimal print thickness of 0.4 mm (depending on the material properties of the filaments) could be achieved. However, the human fingertip consists of tissue of smaller thickness. In this experimental study, a few initial print tests with multi-filament (i.e., PLA and TPU) for the 3D printed features were performed. However, printing multiple material properties without interlocking features led to a crumbling structure. Since the smallest print size was already used for the 3D printed features in question, the printing of two different materials with interlocking features was not feasible and has not been studied further.

Second, μ_s was observed to increase with increasing wavelength *λ*. The wavelength determines the room for deformation of the 3D printed features. However, a positive correlation between the number density of the features and the friction has been observed. Increasing the *λ* furthermore will result in a decreased number density of the 3D printed features, thus decreasing the adhesion-term of the overall friction.

Third, μ_s was observed to decrease under increasing normal load F_n. Discussed in Chapter 2, the theoretical friction model for a contact mechanism with a deformable surface includes an adhesion term $\mathrm{F_{f,adh}}$ and a deformation term $\mathrm{F_{f,adh}}$:

$$\mu_s = \left(\mathrm{F_{f,adh}} + \mathrm{F_{f,def}}\right)/\mathrm{F_n} \qquad (11)$$

When compressed, the 3D printed patterns are flattened. The flattened features limit further deformation of the 3D printed patterns, which increase the overall pattern' stiffness and resulted in an almost rigid contact condition. Therefore, the decrease in μ_s under increasing F_n can be explained due to the fact that $\mathrm{F_{f,def}}$ contributes less-and-less to the overall friction.

Fourth, it was observed that 3D printed features that were aligned in curves with peaks in the opposite direction, such as a wave or circular pattern, generated a higher μ_s compared to the distribution of the features in straight patterns of pillars or lines. These circular patterns resemble a simplified fingerprint pattern of the human fingertip.

Lastly, the highest μ_s was observed between the 3D printed patterns and the fine sandpaper P600. It is highly plausible that the asperities of sandpaper resulted in an addition interlocking, in which the deformation-term increases the overall μ_s. In contrast, it was observed that the μ_s was the lowest for the glass countersurface. It is plausible that the far smaller (micro/nano)asperities of the glass surface did not lead to any additional interlocking, which resulted in an adhesion-dominant friction.

The 3D printed patterns were initially printed on a flat, rectangular, and rigid surface. However, the patterns were designed with the idea of future integration with 3D printed prosthetic hands. To test the effects of the patterns directly on a prosthetic hand, a chosen pattern was printed onto a hollow, glove-liked fingertip structure. These hollow structures could be slid onto the fingertip of the 3D printed prosthetic hands considered in this study [4]. The patterns were printed on a flat, oval and, slightly less rigid fingertip surface. The fingertips were assessed using the Box and Blocks Test (BBT) [46]. The prosthetic users were asked to move as many blocks as possible, one-by-one, from one container to the other, within 60 seconds. The original fingertip design of the prosthetic hand consisted of the rigid PLA material. The grip action of the original design was compared with three different 3D printed fingertips made from the flexible TPU: a flat fingertip; a fingertip with the pattern d00901 (d_1 = 0.4 mm); and a fingertip with the pattern d00911 (d_2 = 0.8 mm). The fingertip pattern d00901 (d_1), showed the highest score of an ~70% increase in the number of blocks moved, compared to the original rigid fingertip of the 3D printed prosthetic hand. The deformable 3D printed patterns were observed to shape around the blocks, thus increasing the fingertips ability to grasp the blocks in more different ways compared to the original rigid fingertips.

11.4. Future Recommendations

The proposed fingertip pattern showed a first step in the direction of improving the grip action of low-cost 3D printed prosthetic hands. However, further research and development are necessary, especially for the FMD 3D print process of flexible materials. In Chapter 3, different bio-inspired design principles have been discussed that influence the contact mechanism between one (or two) deformable surface(s). First, a deformable surface can increase the contact area under load. The adaptability to shapes (e.g., due to the soft finger pad as well as the configuration of the human finger) is believed to increase the grip strongly. Second, normal forces in various directions can be achieved, increasing the grip. Lastly, the role of surface topography, its direction-dependent pattern deformation, and gradients in mechanical properties on the grip force, were discussed. This experimental study mainly focused on analysing the frictional characteristics of 3D printed (deformable) surface topographical patterns. Future research should investigate the possibility of greater shape adaptability at the finger(tip) to improve the grip action of 3D printed prosthetic hands.

The 3D printed features were printed on a flat surface. The next step could be to integrate the surface topographical patterns with an underlying fingertip shape and structure that bio-mimics the adaptability of the human fingertip. The first step could be by creating (semi-)hollow finger pad structures of a flexible material to mimic the soft tissue of the finger pulp.

Moreover, the 3D printed patterns in this study were generally printed vertically to the build plate because printing in different angles resulted in holes or gaps in the layers for the smallest print thickness. However, considering that the fingertip patterns are designed to be integrated into a 3D printed prosthetic hands, it might not be always feasible to print the patterns in a straight vertical line. Therefore, further research is needed on the effect on dimensional accuracy when printing at an angle (i.e., instead of vertical) due to the so-called ‘staircase effect’.

The 3D printed prosthetic hands, used in this experiment, is based on a non-assembly design approach. Considering that the soft, TPU fingertips will be integrated into the original, rigid PLA design of the 3D printed prosthetic hands, further research is necessary on the 3D printing of two different material properties in a single print production process.

Lastly, further investigations should aim to study the durability and reliability of the small dimensioned 3D printed features. A basic user test is recommended, in which the fingertips can be tested in a more natural setting, i.e., daily used objects and countersurfaces.

12. CONCLUSION

Commercial prosthetic hands are still limited in their grasping ability, such as the adaptability to the shape of an object and a sufficient pinch force level for practical use. The goal of this experimental study is to engineer a bio-inspired surface structure to improve the grip action of prosthetic hands and to evaluate the FDM 3D printing technology for this purpose. 3D printed prosthetic hands, generally consist of rigid materials. On the contrary, human fingertips and various biological adhesive surface consist of deformable surface structures. These deformable structures allow for adaptability and uniform distribution of stress. To analyse the contact mechanism of deformable 3D printed surface features, the flexible and abrasion-resistant Thermoplastic Polyurethane (TPU) 95A Red was used. The 3D printed (deformable) features were printed on top of a rigid, rectangular surface. The 3D printed features consisted of pillars or lines with varying thickness *d*, tip thickness *D*, wavelength λ, and curvatures α that were combined into different patterns. The flexible TPU showed various challenges when it came to small dimension printing with the FDM 3D printer, Ultimaker 3, such as the large discrepancy in printing accuracy, the occasional holes or gaps in the printed layers, and sensitivity to the print speed. The latter occasionally resulted in the compression of the material, jamming of the material in the 3D printer's print head, and strings of material between parts of the original design. The 3D printed surface patterns were tested against three different countersurfaces: glass (smooth), sandpaper P240 (rough), and sandpaper P600 (fine).

Despite the small differences in the static coefficient of friction μ_s of the 3D printed patterns, some consistent trends were found. First, μ_s increases with increasing thickness *d*. Second, μ_s increases with increasing wavelength λ up to a point in which the decrease of number density decreases the overall friction. Third, μ_s decreases under increasing normal load F_n. Fourth, μ_s increases for pattern curvatures with peaks in the opposite direction, such as wave or circular patterns. Lastly, a higher μ_s was observed against the sandpaper countersurface, compared to the glass countersurface. To test the effects of the patterns directly on a prosthetic hand, a chosen pattern was printed onto a hollow, glove-liked fingertip structure which could be slid onto the fingertip of the 3D printed prosthetic hands considered in this study. The fingertips were assessed using the Box and Blocks Test (BBT), in which the pattern with the highest score displayed an ~70% increase in the number of blocks moved, compared to the original rigid fingertip of the prosthetic hand. The deformable 3D printed patterns were observed to shape around the blocks, thus increasing the fingertips ability to grasp the blocks in more different ways compared to the original rigid fingertips.

Further research and development is essential, especially for the FMD 3D print process of small dimensional printing in combination with flexible materials. Further research must also include the analysis of the optimal pattern height *h*, the integration of the surface patterns with an underlying structure that displays greater shape adaptability, the printing of two different material properties; i.e. the flexible TPU fingertips onto the rigid PLA prosthetic hand, and lastly, a durability test of the small 3D printed features.

Nevertheless, the proposed fingertip pattern demonstrated a first step towards future improvements of the grip action of low-budget 3D printed prosthetic hands using soft fingertip patterns.

BIBLIOGRAPHY

[1] What is 3D Printing? (n.d), *3dprinting,* [Accessed Apr. 2019], url: https://3dprinting.com/what-is-3d-printing.

[2] Gibson, I., Rosen, D., Stucker, B. (2015). Additive Manufacturing Technologies, 2nd edn., *Springer,* ISBN 978-1-4939-2113-3, 498 p. doi: https://doi.org/10.1007/978-1-4939-2113-3.

[3] Ibrahim, A., et al. (2015). Three-dimensional Printing in Developing Countries, *Plastic and Reconstructive Surgery,* 3:7, doi: 10.1097/GOX.0000000000000298.

[4] Cuellar, J. S., et al. (2018). Ten guidelines for the design of non-assembly mechanisms: The case of 3D-printed prosthetic hands, *Proceedings of the Institution of Mechanical Engineers, Part H: Journal of Engineering in Medicine,* 232:9, pp. 962-971, doi: https://doi.org/10.1177/0954411918794734.

[5] Dechev, N., Cleghorn, W.L., Naumann, S. (2001). Multiple Finger, Passive Adaptive Grasp Prosthetic Hand, *Mechanism and Machine Theory,* 36:10, pp. 1157-1173, doi: https://doi.org/10.1016/S0094-114X(01)00035-0.

[6] Carrozza, M., et al. (2005). A Cosmetic Prosthetic Hand with Tendon Driven Under-Actuated Mechanism and Compliant Joints: Ongoing Research and Preliminary Results, *IEEE International Conference on Robotics and Automation,* pp. 2661-2666, doi: https://doi.org/10.1109/ROBOT.2005.1570515.

[7] Van Der Heide, E., Zeng, X., Masen, M. (2013). Skin tribology: Science friction?, *Friction,* 1:13, pp. 130-142, doi: https://doi.org/10.1007/s40544-013-0015-1.

[8] Barnes, C., et al. (2004). Surface finish and touch. A Case Study In a New Human Factors Tribology, *Wear,* 7-8, pp. 740-750, doi: https://doi.org/10.1016/j.wear.2004.03.018.

[9] Shao, F., Childs, T.H.C., Henson, B. (2009). Developing an Artificial Fingertip with Human Friction Properties, *Tribology International,* 42: 11-12, pp. 1575-1581, doi: https://doi.org/10.1016/j.triboint.2009.02.005.

[10] Schreuders, T., Brandsma, J., Stam, H. (2014). Hand Function. A Practical Guide to Assessment, *Springer,* pp. 3-22, doi: https://doi.org/10.1007/978-1-4614-9449-2.

[11] Science Source (2013). Hand And Wrist Bones, *FineArtAmerica,* [Accessed 2019], url: https://fineartamerica.com/featured/3-hand-and-wrist-bones-science-source.html.

[12] Watanabe, T., Harade, K., Tada, M. (2018). Hand Design: Hybrid Soft and Hard Structures Based on Human Fingertips for Dexterity. In: Watanabe, T., *Human Inspired Dexterity in Robotic Manipulation. Academic Press,* chap. 7, pp. 115-147. doi: https://doi.org/10.1016/B978-0-12-813385-9.00007-8.

[13] Onumah, N., Jeyakumar, A. (2019) Nail Surgery, *Medscape,* [Accessed 2019], url: https://emedicine.medscape.com/article/1126725-overview.

[14] Wortsman, X. (2018). Normal Ultrasound Anatomy of the Skin, Nail, and Hair, *Atlas of Dermatologic Ultrasound, Springer,* pp. 1-22, doi: https://doi.org/10.1007/978-3-319-89614-4_1.

[15] Wilkinson, P.F., Millington, R. (1983). Skin. Biological Structure and Function, *Cambridge University Press,* pp. 49-50. ISBN 0521241227.

[16] Controzzi, M., et al. (2014). Bioinspired Fingertip for Anthropomorphic Robotic Hands, *Applied Bionics and Biomechanics, IOS Press,* vol 11, pp. 25-38, doi: 10.3233/ABB-140092.

[17] Zhang, S., et al. (2015). The Role of the Sliding Direction Against a Grooved Channel Texture on Tool Steel: An Experimental Study on Tactile Friction, *International Journal of Solids and Structures,* vol. 56–57, pp. 53–61, doi: https://doi.org/10.1016/j.ijsolstr.2014.12.005.

[18] Newman, T. (2018). Skin: How it works., *Medical News Today,* [Accessed 2019], url: https://www.medicalnewstoday.com/articles/320435.php.

[19] Rodríguez, A., et al. (2016). Modelling the Static Contact Between a Fingertip and a Rigid Wavy Surface, *Tribology International,* vol. 102, pp. 114-124, doi: https://doi.org/10.1016/j.triboint.2016.05.028.

[20] Maltoni, D. (2009). Fingerprint Analysis and Representation. In: Maltoni, D., *Handbook of Fingerprint Recognition. Springer,* pp. 83-130, doi: 10.1007/978-1-84882-254-2.

[21] Kucken, M. (2007). Models for Fingerprint Pattern Formation, *Forensic Science International,* 171:2-3, pp. 85-96, doi: https://doi.org/10.1016/j.forsciint.2007.02.025.

[22] Moayer, B., and Fu, K. S. (1975). A Syntactic Approach to Fingerprint Patern Recognition, *Pattern Recognition,* 7:1-2, pp. 1-23, doi: https://doi.org/10.1016/0031-3203(75)90011-4.

[23] Malassiotis, S. (2009). Finger Geometry, 3D. In: Li, S. Z., Jain, A., *Encyclopedia of Biometrics. Springer,* ISBN 978-0-387-73002-8, doi: https://doi.org/10.1007/978-0-387-73003-5_250.

[24] Dzidek, B., et al. (2017). Why Pens have Rubbery Grips, *PNAS National Academy of Sciences,* 114:41, pp. 10864-10869, doi: https://doi.org/10.1073/pnas.1706233114.

[25] Delhaye, B., et al. (2016). Surface Strain Measurements of Fingertip Skin Under Shearing, *Journal of the Royal Society Interface,* 13:115, doi: https://doi.org/10.1098/rsif.2015.0874.

[26] Delhaye, B., Lefèvre, P., Thonnard, J.-L. (2014). Dynamics of Fingertip Contact During the Onset of Tangential Slip, *Journal of the Royal Society Interface,* 11:100, doi: https://doi.org/10.1098/rsif.2014.0698.

[27] Brely, L., et al. (2017). Optimal Adhesion Control via Cooperative Hierarchy, Grading, Geometries and Non-linearity of Anchorages and Adhesive Pads. In: Heepe, L., et al., *Bio-inspired Structured Adhesives. Springer,* chap. 6, pp. 81-93, doi: https://doi.org/10.1007/978-3-319-59114-8.

[28] Heepe, L., et al. (2017). Impact of Ambient Humidity on Traction Forces in Ladybird Beetles (Coccinella septempunctata). In: Heepe, L., et al., *Bio-inspired Structured Adhesives. Springer,* chap. 2, pp. 21-32, doi: https://doi.org/10.1007/978-3-319-59114-8.

[29] Tan, D., Zheng, Y., Xue, L., (2017). The Role of Effective Elastic Modulus in the Performance of Structured Adhesives. In: Heepe, L., *Bio-inspired Structured Adhesives. Springer,* chap. 8, pp. 107-139, doi: https://link.springer.com/book/10.1007/978-3-319-59114-8.

[30] Friction. Learn more about Friction, *ScienceDirect,* [Accessed 2019], url: https://www.sciencedirect.com/topics/materials-science/friction.

[31] Qiu, M. et al. (2017). Bearing Tribology. Principles and Applications, *Springer,* ISBN 978-3-662-53095-5, doi: https://doi.org/10.1007/978-3-662-53097-9.

[32] Surface Topography. Learn more about Surface Topography., *ScienceDirect,* [Accessed Febr. 2019], url: https://www.sciencedirect.com/topics/materials-science/surface-topography.

[33] Zappone, B., Rosenberg, K., Israelachvili. J. (2007). Role of Nanometer Roughness on the Adhesion and Friction of a Rough Polymer Surface and a Molecularly Smooth Mica Surface, *Tribology Letters,* 26:191, doi: https://doi.org/10.1007/s11249-006-9172-y.

[34] Schematic Diagram of Surface Charactersistics., *Constructioncanada,* [Accessed Apr. 2019], url: https://www.constructioncanada.net/concrete-floors-does-sealed-mean-the-same-thing-as-polished/schematic-diagram-of-surface-characteristics/.

[35] Heepe, L., et al. (2017). Hierarchical Models of Engineering Rough Surfaces and Bio-inspired Adhesives. In: Borodich, F.M., Savencu, O., *Bio-inspired Structured Adhesives. Springer,* chap. 10, pp. 79-219, Online ISBN 978-3-319-59114-8, doi: https://doi.org/10.1007/978-3-319-59114-8_10.

[36] Van Kuilenburg, J., Masen, M.A., Van Der Heide, E. (2015). A Review of Fingerpad Contact Mechanics and Friction and How This Affects Tactile Perception, *Proceedings of the Institution of Mechanical Engineers, Part J: Journal of Engineering Tribology,* 229:3, pp. 243-258, doi: https://doi.org/10.1177/1350650113504908.

[37] Stachowiak, G.W., Batchelor, A.W. (1993). Fundamentals of Contact Between Solids, *Engineering TriBology. Elsevier BV,* chap. 10, vol 24, pp. 527-556, doi: https://doi.org/10.1016/S0167-8922(08)70584-4.

[38] Adams, M.J., et al. (2013). Finger Pad Friction and Its Role in Grip and Touch, *Journal of the Royal Society Interface,* 10:20120467, doi: http://dx.doi.org/10.1098/rsif.2012.0467.

[39] Tomlinson S.E., Lewis, R., Carré, M.J. (2009). The Effect of Normal Force and Roughness on Friction in Human Finger Contact, *Wear. ScienceDirect,* 267:5-8, pp. 1311–1318, doi: https://doi.org/10.1016/j.wear.2008.12.084.

[40] Derler, S., (2009) Friction of Human Skin Against Smooth and Rough Glass as a Function of The Contact Pressure, *Tribology International, ScienceDirect,* 42:11-12, pp. 1565–1574, doi: https://doi.org/10.1016/j.triboint.2008.11.009.

[41] Derler, S., Gerhardt, L.C. (2012). Tribology of Skin: Review and Analysis of Experimental Results for the Friction Coefficient of Human Skin, *Tribology Letters, Springer,* 45:1, pp. 1-27, doi: https://doi.org/10.1007/s11249-011-9854-y.

[42] Dzidek, B., et al. (2016) Frictional Dynamics of Finger Pads are Governed by Four Length-Scales and Two Time-Scales, *IEEE Haptics Symposium,* pp. 161-116, doi: 10.1109/HAPTICS.2016.7463171.

[43] Advanced 3D printing materials: The choice is yours., *Ultimaker,* [Accessed 2019], url: https://ultimaker.com/materials.

[44] Coefficient of Friction Testing. Ametektest., *Ametektest,* [Ametektest 2019], url: https://www.ametektest.com/learningzone/testtypes/coefficient-of-friction-testing.

[45] Cuellar, J.S., et al. (2019). Functional Evaluation of a Non-assembly 3D-printed Hand Prosthesis, *Proceedings of the Institution of Mechanical Engineers, Part H: Journal of Engineering in Medicine,* 233:11, doi: https://doi.org/10.1177%2F0954411919874523.

[46] Mathiowetz, V. (1985). Adult Norms for The Box and Block Test of Manual Dexterity, *American Journal of Occupational Therapy,* vol. 39, 386 p., doi: 10.5014/ajot.39.6.386/.

[47] Jackson, B. (2018). Researchers Achieve Breakthrough For Industrial-Scale Nano-3D Printing, *3dprintingindustry,* [Accessed 2019], url: https://3dprintingindustry.com/news/researchers-achieve-breakthrough-for-industrial-scale-nano-3d-printing-163002/.

[48] Ultimaker S3 technical specifications., *Ultimaker,* [Accessed 2019], url: https://ultimaker.com/3d-printers/ultimaker-s3.

[49] Meyers M.A., Chen P.Y., Lin A.Y.M., Seki Y. (2008).Biological materials: Structure and mechanical properties, *Progress in Materials Science,* 53:1, pp. 1-206, doi: https://doi.org/10.1016/j.pmatsci.2007.05.002.

APPENDIX

A. Final Print Setting: Ultimaker 3

The 3D printed objects were printed using the slicing software Cura 4.1, the Ultimaker 3 FDM 3D printer, and a 0.4 mm nozzle.

Category	Setting	Value
Quality	Layer Height	0.15 mm
Shell	Wall Thickness	0.76 mm
	Wall Line Count	2
	Top/Bottom Thickness	0.7 mm
	Top Thickness	0.7 mm
	Top Layers	5
	Bottom Thickness	0.7 mm
	Bottom Layers	5
	Horizontal Expansion	0
Infill	Infill Density	10
	Infill Pattern	Triangles
Material	Printing Temperature	225 °C
	Build Plate Temperature	60 °C
	Enable Retraction	On
Speed	Print Speed	15 mm/s
Travel	Z Hop When Retracted	On
Cooling	Enable Print Cooling	On
	Fan Speed	20%
Support	Generate Support	Off
Build Plate Adhesion	Enable Prime Blob	On
	Build Plate Adhesion Type	Brim
	Build Plate Adhesion Extruder	Extruder 2 (TPU A95)
	Brim Width	6 mm
Dual Extrusion	Enable Prime Tower	On
	Prime Tower X Position	177.07 mm
	Prime Tower X Position	185.924 mm

Figure A.1. Printer setting in Cura

B. Dimensions of the 3D Printed Test Equipment

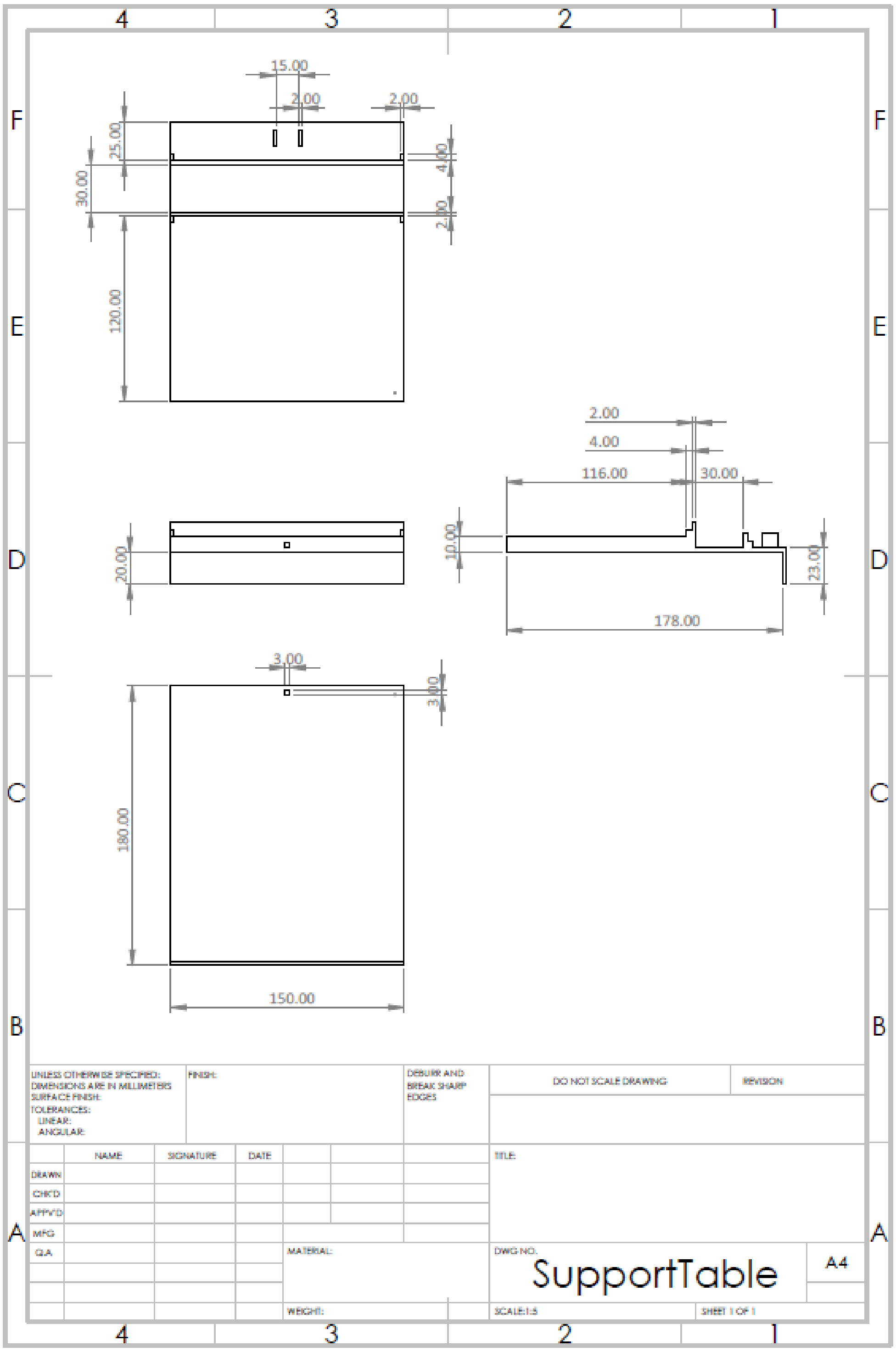

Figure B.1. Dimensions of the 3D CAD Model of the Support-Table.

C. Dimensions of the 3D Printed Pattern d00901

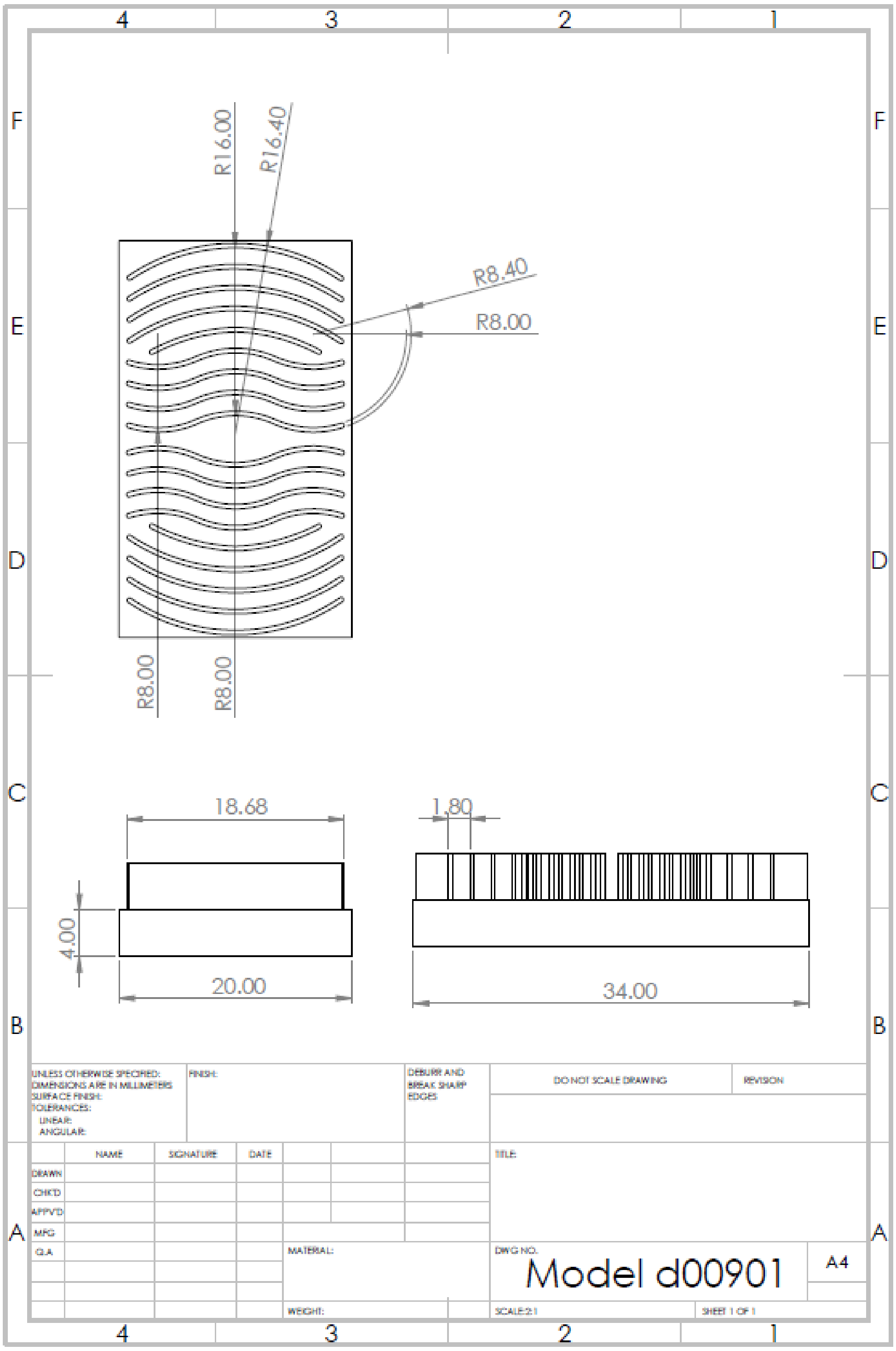

Figure C.1. Dimensions of the 3D CAD Model Pattern d00901.

D. Dimensions of the 3D Printed Index Finger with Pattern d00901

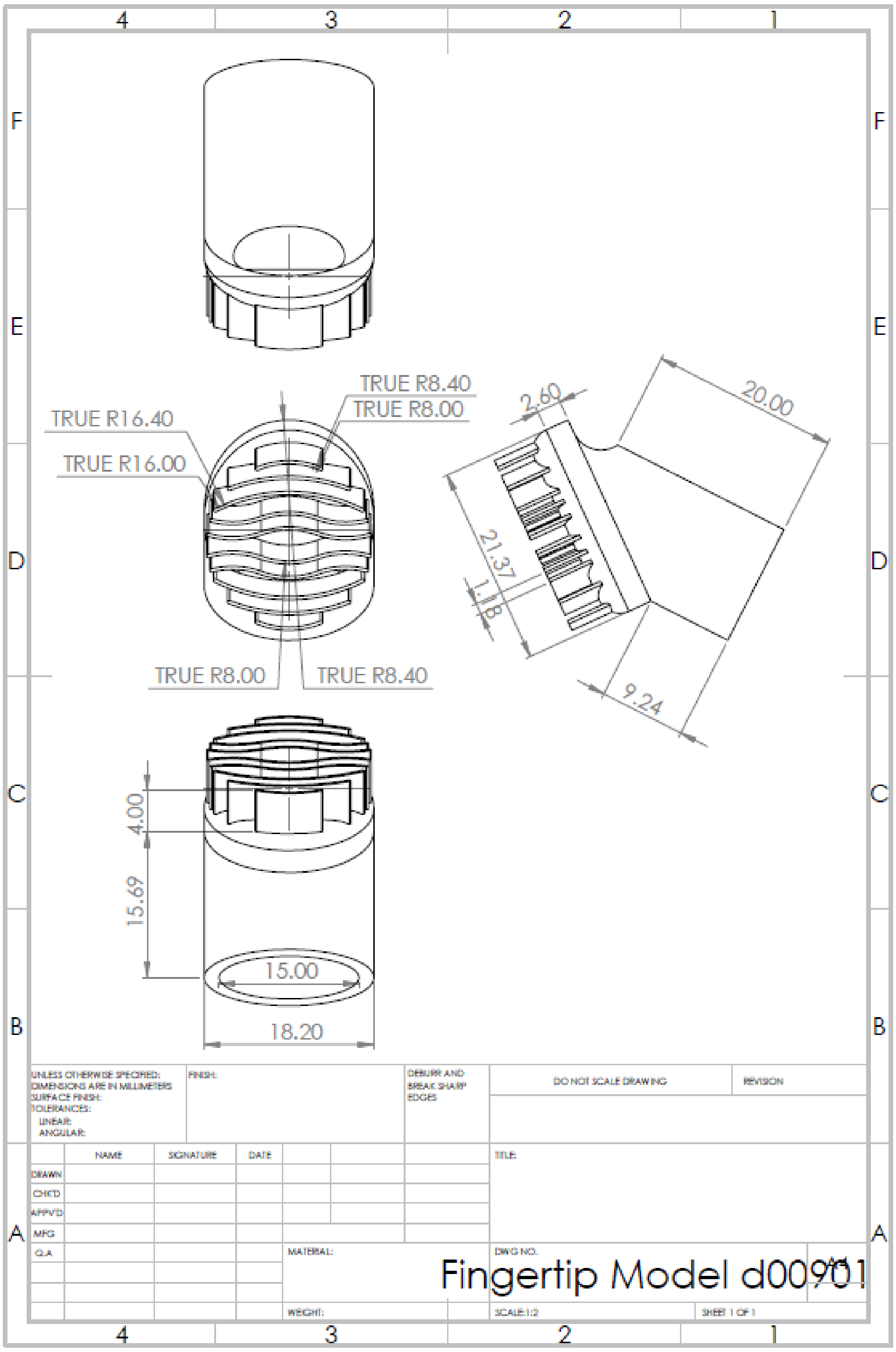

Figure D.1. Dimensions of the 3D CAD Model: Index Fingertip with Pattern d00901.